Functional Optical Coherence Tomography of Stimulus-Evoked Intrinsic Optical Signals in the Retina

BY

BENQUAN WANG
B.E., Tianjin University, 2012

THESIS

Submitted as partial fulfillment of the requirements
for the degree of Doctor of Philosophy in Bioengineering
in the Graduate College of the
University of Illinois at Chicago, 2017

Chicago, Illinois

Defense Committee:

Xincheng Yao, Chair and Advisor
David Pepperberg, Ophthalmology and Visual Sciences
Dieter Klatt, Bioengineering
Dingcai Cao, Ophthalmology and Visual Sciences
John Hetling, Bioengineering

ACKNOWLEDGMENTS

I would like to express my deepest gratitude to my respectable advisor Dr. Xincheng Yao, for his valuable instructions for my research. He has been a tremendous mentor for me. In the past five years, he always provides insightful guidance as well as sincere and warm support to encourage me to grow as a research scientist. His advices on both my research and career have been so precious to me.

I would also like to thank Dr. David Pepperberg, Dr. Dieter Klatt, Dr. Dingcai Cao, and Dr. John Hetling for being willing to serve as my committee members. I really appreciate them for the valuable comments and suggestions on my research.

I would like to thank my colleagues, Dr. Changgeng Liu, Yiming Lu, Dr. Devrim Toslak, Dr. Taeyoon Son, and Minhaj Alam. They have helped me a lot in research and in life. It was a great time and experience working with all the brilliant colleagues. I would also like to thank previous colleagues, Dr. Rongwen Lu and Dr. Qiuxiang Zhang. They are good friends in life and were good teachers in work. They helped me and taught me a lot when I first joined Dr. Yao's lab, and helped me start my research career.

Special thanks to my family for their unfailing and continuous support even they're far across the Pacific Ocean. Thank my parents for their selfless love. I would also like to give my deepest thanks to my beloved wife. She is the most wonderful gift from God. She is always supporting and comforting me and is always taking care of me so well. She cooks for me every day and always keeps our home clean, warm and cozy. She is always there for me through the good and bad times. I cannot thank her enough for encouraging me going through this experience.

B.W.

TABLE OF CONTENTS

TABLE OF CONTENTS (continued)

CONTRIBUTION OF AUTHORS

Chapter II [1], III [2] and IV [3] are published manuscripts in which I was the primary author. I was responsible for designing the experiment, building the imaging system, acquiring data, processing data and writing the manuscript. Dr. Xincheng Yao supervised the projects, and contributed to experiment design, data processing, and manuscript writing. In Chapters II and III, Dr. Rongwen Lu helped with experiment design and data processing and Dr. Qiuxiang Zhang helped with imaging system development. In Chapter II, Dr. Yuqiang Jiang provided insightful comments about the results. In Chapter IV, Yiming Lu helped with imaging system design and animal preparation.

Chapter V is a manuscript submitted to Investigative Ophthalmology & Visual Science and under review. I contributed to system design, prototype construction, data acquisition and manuscript preparation. Yiming Lu helped with animal preparation and provided advice on interpretation of results. Dr. Taeyoon Son helped with data processing. Dr. Xincheng Yao supervised this project, and contributed to system design, experimental design, data analysis, and manuscript preparation.

LIST OF FIGURES

LIST OF FIGURES (continued)

LIST OF ABBREVIATIONS

AMD	Age-related macular degeneration
AO	Adaptive optics
CCD	Charge-coupled device
cGMP	Cyclic guanosine monophosphate
DR	Diabetic retinopathy
ELM	External limiting membrane
EM	Electron microscope
EOPM	Electro-optic phase modulator
ERG	Electroretinogram
FWHM	Full width half maximum
GCL	Gangling cell layer
GMP	Guanosine monophosphate
ILM	Internal limiting membrane
INL	Inner nuclear layer
IOS	Intrinsic optical signal
IPL	Inner plexiform layer
IS	Inner segment
ISe	Inner segment ellipsoid
LED	Light emitting diode
LS-OCT	Line-scan optical coherence tomography
NA	Numerical aperture
NFL	Nerve fiber layer
NIR	Near infrared
OCT	Optical coherence tomography

LIST OF ABBREVIATIONS (continued)

ONL	Outer nuclear layer
OPL	Outer plexiform layer
OS	Outer segment
PDE	Phosphodiesterase
PN	Postnatal day
rd10	Retinal degeneration 10
RP	Retinitis pigmentosa
RPE	Retinal pigment epithelium
SCE	Stiles-Crawford effect
SD-OCT	Spectral domain optical coherence tomography
SLD	Superluminescent diode
SLO	Scanning laser ophthalmoscope
SNR	Signal-to-noise ratio
TD-OCT	Time domain optical coherence tomography
TRP	Transient retinal phototropism
WT	Wild type

SUMMARY

Retinal diseases, such as age-related macular degeneration (AMD) [4, 5], retinitis pigmentosa (RP) [6], diabetic retinopathy (DR) [7, 8] and Glaucoma [9, 10], can ultimately lead to severe to total vision loss if not diagnosed and treated timely. Fundus examination using conventional optical instruments like fundus camera and optical coherent tomography (OCT) cannot directly reveal functional distortions of retinal physiology before detectable morphological abnormalities. Functional examination methods like electroretinogram (ERG) [11] suffer from low spatial resolution. Concurrent morphological and functional examination is desirable for early detection of retinal diseases. Intrinsic optical signal (IOS) promises an imaging method that provides high-resolution functional imaging of retinal physiology, allowing simultaneous assessment of retinal morphology and function.

IOS represents optical property changes in the stimulus activated retina. In previous studies, we demonstrated robust IOS changes in both isolated and *in vivo* frog retinas [12-14]. Both fast and slow IOSs were observed [15, 16]. Our studies, as well as studies in other labs, demonstrated the potential of IOS as a unique biomarker for retinal disease detection. However, anatomic and physiological mechanisms of retinal IOSs are still not well understood, and the correlation between IOS distortions and retinal pathologies are not well established yet.

This dissertation research is designed to develop a systematic understanding of IOS, explore the characteristics of normal IOS, understand the mechanism of IOS and test the feasibility of IOS in retinal diseases diagnosis. Different studies that utilized specially designed imaging systems and animal models were conducted for this dissertation research.

To study characteristics of normal IOS in frogs and mice, a line-scan OCT (LS-OCT) and an *in vivo* spectral domain OCT (SD-OCT) were built. Using the LS-OCT, fast IOS from photoreceptor outer segment (OS) of isolated frog retina was selectively obtained. Results showed mixed

SUMMARY (continued)

positive and negative fast IOSs confined in the stimulated area. The onset-time and half-peak-time of fast IOS in frogs were <3 ms and <10 ms [1]. Using the *in vivo* SD-OCT, IOS from intact mouse retina was studied under different stimulation conditions. Fast IOS was mainly observed from OS and slow IOS was observed from inner plexiform layer (IPL). The response of fast IOS to stimulation intensity changes was similar to the response of ERG a-wave, i.e., as stimulation intensity increased, the amplitude increased and time course decreased [3].

The IOS imaging in isolated frog retinas and intact mouse retinas also revealed the physiological mechanism of fast IOS. In the isolated frog retinas, it was observed that onset time of negative fast IOS was shorter than that of positive fast IOS. We suspect that negative and positive fast IOSs may involve different processes in phototransduction, i.e. the G-protein binding and releasing processes [1]. From intact mouse retinas, it was observed that onset time of fast IOS was significantly shorter than onset time of ERG a-wave. Since ERG a-wave is generated by photoreceptor hyperpolarization, it suggested that fast IOS was generated by the processes before hyperpolarization of photoreceptor [3].

To understand the dynamical mechanism of fast IOS, a hybrid imaging system that combined line-scan confocal microscope and SD-OCT was built to study the rod phototropism. Phototropism is the phenomenon that when an oblique light is delivered to the photoreceptor, photoreceptor rapidly moves towards the light. Results showed that phototropism was observed only in photoreceptor OS, thus it is the main contributor to fast IOS observed in OS [2].

With the developed understanding of normal IOS, a study using SD-OCT was conducted to assess how IOS was affected by retinal diseases. IOS was imaged from retinal degeneration 10 (rd10) mice from postnatal day 15 (P15) to P21. Results showed that fast IOS could identify retinal dysfunction at P16 when no statistically significant retinal thickness change could be

SUMMARY (continued)

observed from OCT images yet. This study demonstrated the feasibility of using fast IOS to do early detection of retinal diseases, and paved way for more animal studies using different diseased models.

In summary, this dissertation research advanced our understanding of IOS, established the foundation for further research on IOS with different diseased mouse models, and paved the way for adapting IOS as a new high resolution functional diagnostic tool for retinal diseases in clinic.

CHAPTER I. INTRODUCTION

Retinal diseases, e.g. age-related macular degeneration (AMD) [4, 5], retinitis pigmentosa (RP) [6], diabetic retinopathy (DR) [7, 8] and glaucoma [9, 10], can produce retinal neural dysfunction and lead to total vision loss if proper treatment was not conducted timely. Different retinal cells that are located in different retinal layers are vulnerable to different retinal diseases. For example in the early stage of AMD development rods first degenerate [4], but there are no reliable tools for detecting early rod dysfunction. Morphological imaging tools, e.g. fundus photography and optical coherence tomography (OCT) [17], show high resolution morphological structures of the retina but cannot detect retinal dysfunction that appears before morphological changes can be detected. Functional evaluation methods, e.g., electroretinogram (ERG) [11] and multifocal ERG [18, 19] have limited spatial resolution, and thus cannot locate the specific area with degenerated cells. Furthermore, sometimes it is difficult to interpret the ERG outcome due to complex involvements of multiple types of retinal cells on the electrophysiological measurement. Thus, high resolution mapping of retinal physiological function is desirable for improved retinal disease diagnosis. Based on high resolution imaging and dynamic differential data processing, intrinsic optical signal (IOS) is closely related to functional activities of the retina. Therefore, functional IOS imaging could potentially be a powerful tool for objective assessment of retinal diseases. However, clinical application of IOS is still challenging because of limited knowledge about the mechanism of IOS, and the relationship between IOS and retinal diseases. This dissertation research is designed to improve our understanding about IOS and study IOS distortions in mutant animal models, and thus pave the way toward clinical application of functional IOS imaging.

In this chapter, background information of this dissertation research is first provided. The retina is the sample used in this dissertation research. Phototransduction is the process in the retina that turns light signal into electrical signal. The electric signal is then transmitted to the brain.

The electric activity recorded from the retina is called ERG. ERG is a widely used functional diagnosing tool which reflects the functionality of the retina and different retinal cells. Another widely used diagnosis tool in eye clinic is OCT. OCT provides high resolution images of the retina that show clearly the layered structure. In coordination with visible light stimulation, near infrared light functional OCT is the main imaging modality used in this dissertation research for IOS imaging.

After the background information, the topic of this dissertation research is discussed. This research focused on improving our understanding of IOS, and testing the feasibility of using fast IOS to track retinal disease progression. Both frog and mouse retinas were used for this study. Different imaging systems were designed and built for retinal imaging, including a line-scan OCT (LS-OCT), a hybrid imaging system that combines confocal microscope and spectral domain OCT (SD-OCT), and an *in vivo* SD-OCT. With these studies, spatiotemporal characteristics and biophysical mechanisms of IOS were investigated, and the potential of functional IOS mapping of diseases associated retinal neural dysfunction was demonstrated.

1.1 Background

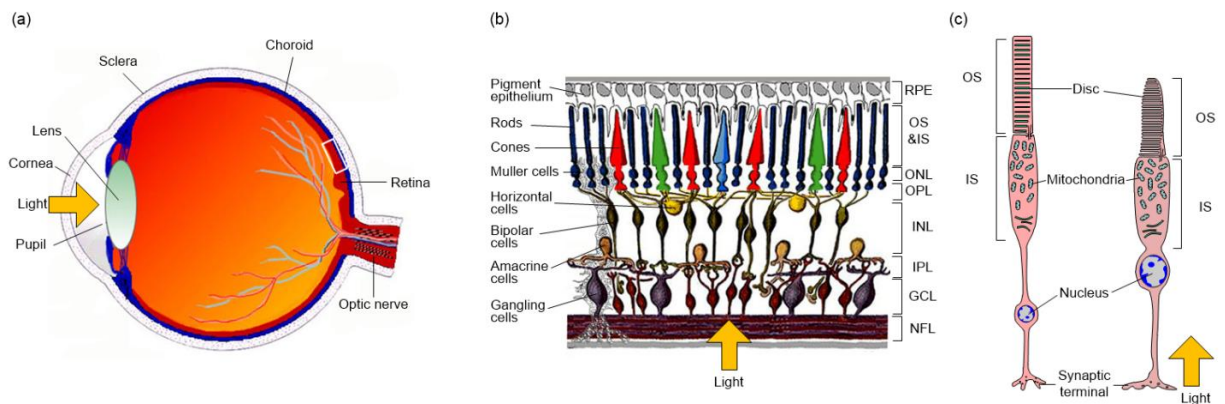### 1.1.1 The retina

Fig. 1.1 Anatomy of the eye, retina, and photoreceptors. (a) Cartoon showing cross-sectional eyeball image with major structures labeled. (b) Cartoon of the retina with major cell types and layers marked. (c) Cartoon of rod and cone photoreceptors. (a) is reprinted from [20] with permission; (b) is reprinted from [21] with permission; (c) is reprinted from [22] with permission.

The retina is the inner most layer of the eye. Image is formed on the retina through the optics [cornea, crystalline lens, and aqueous humor, etc. (Fig. 1.1a)] of the eye. The image is then converted to electric signals by photoreceptor cells, and photoreceptor cells send the electric signal to downstream retinal cells and then to the brain via nerve bundles. The retina is composed of different highly organized cells, as shown in Fig. 1.1(b). These cells include photoreceptor cells, bipolar cells, gangling cells, horizontal cells, amacrine cells, and Müller cells, etc. Cell bodies and dendrites of different cells form different retinal layers. As shown in Fig. 1.1(b), these layers include retinal pigment epithelium layer (RPE), photoreceptor outer segment layer (OS), photoreceptor inner segment layer (IS), outer nuclear layer (ONL), outer plexiform layer (OPL), inner nuclear layer (INL), inner plexiform layer (IPL), gangling cell layer (GCL) and nerve fiber layer (NFL) [23]. The RPE layer is composed of pigment epithelium. The OS layer contains photoreceptor OS, and the IS layer contains photoreceptor IS. The ONL is composed of cell bodies of photoreceptor cells. The INL is composed of cell bodies of horizontal cells, bipolar cells, and amacrine cells. The GCL consists of mainly cell bodies of gangling cells, and cell bodies of some displaced amacrine cells. The OPL and IPL are layers of neuropils where synaptic contact with each other. The NFL is composed of axons of gangling cells. The axons pass through the retina at optic nerve head and form optic nerve bundle that goes to the brain.

There are two different photoreceptor cells, rods and cones [Fig. 1.1(c)] [24]. They get their names from their rod and cone shapes. Rods are sensitive to light and are responsible for low light vision. Cones are less sensitive and are responsible for color vision. Cones could be further classified according to the wavelength of light that they are most sensitive to. For example, there are three kinds of cones in human retina, the long, middle and short wavelength cones, which are most sensitive to ~560 nm, ~530 nm and ~420 nm light, respectively [25, 26].

As shown in Fig. 1.1(c) the structure of both rods and cones are similar, despite their different shapes. Both rod and cone cells are consisted of OS, IS, nucleus and synaptic body. The outer

segment is the part that turns photons into electric signal through the process called phototransduction.

1.1.2 Phototransduction
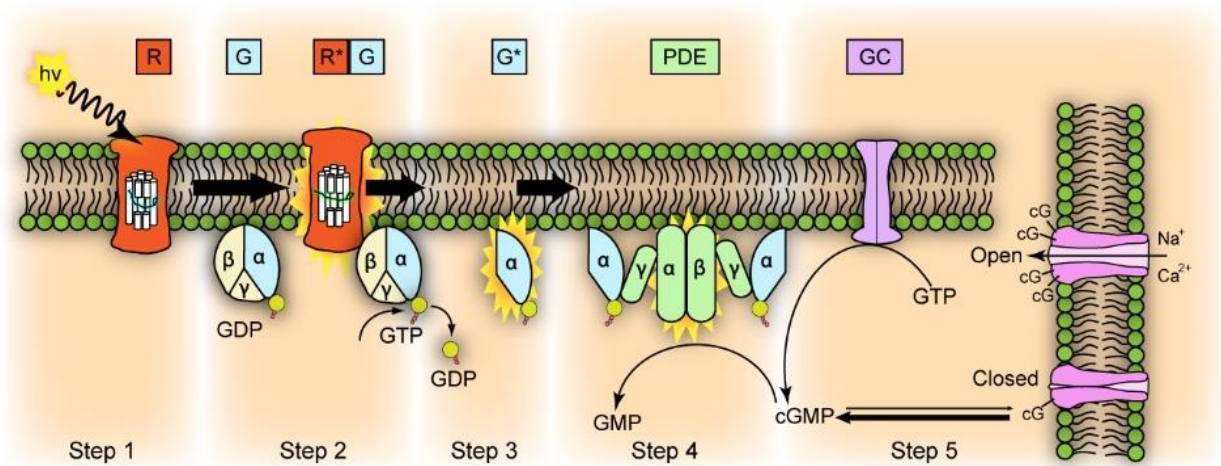
Fig. 1.2 Illustration of phototransduction process. The horizontal membrane is disc membrane; the vertical membrane is photoreceptor OS plasma membrane. Step 1: a photon hits rhodopsin and rhodopsin is activated (R*). Step 2: activated rhodopsin activates transducin (G*). The GDP that binds to α subunit of transducin is replaced by GTP, and the α subunit-GTP complex splits from transducin. Step 3: α subunit-GTP complex activates PDE. Step 4: activated PDE transforms cGMP to GMP. Step 5: Due to the reduced concentration of cGMP, cGMP gated ion channel closes, and photoreceptor becomes hyperpolarized. Reprinted from [27] with permission.

The process that photoreceptor captures photons and creates electrical signal is called phototransduction [28-30]. In rod photoreceptors, the phototransduction process starts from rhodopsin, a transmembrane protein on rod OS discs. When a photon hits the rhodopsin, the 11-cis retinal in the rhodopsin undergoes isomerization and changes to all-trans retinal [31]. All-trans retinal no longer fits the binding site of rhodopsin and rhodopsin is activated [32]. Activated rhodopsin then activates the transducin [33]. The transducin has three subunits, the α, β and γ subunits. The α subunit has GDP bound on. When transducin is activated, it dissociates the GDP from α subunit and binds GTP instead. The α and GTP complex then dissociates from β and γ subunits and activates phosphodiesterase (PDE). Activated PDE then hydrolyzes cyclic

guanosine monophosphate (cGMP) to GMP. This lowers the cGMP concentration thus cGMP gated sodium channels on the photoreceptor cell membrane are closed [34]. The closure of sodium channels causes the hyperpolarization of the photoreceptor cell. The hyperpolarization then closes the voltage gated calcium channels. Then calcium concentration in photoreceptor cell is reduced. Glutamate released by photoreceptor synaptic terminal is in turn reduced. Photoreceptor synaptic is in contact with bipolar cells, thus the visual signal is then transmitted to bipolar cells and then to other downstream retinal cells.

1.1.3 Electroretinogram

ERG measures the integrated electrical activities generated by retinal cells in response to light stimulation [35]. It is a standard tool for evaluating retinal functionality in clinic and provides diagnostic information for a variety of retinal diseases, e.g. retinitis pigmentosa (RP) [36, 37], and congenital stationary night blindness [38, 39]. To record ERG, an active electrode is placed in contact with cornea. A negative electrode is typically placed on the ear lobe. Then a light stimulation is introduced to stimulate the retina. The electrical activities of the retina are then amplified and recorded as ERG.
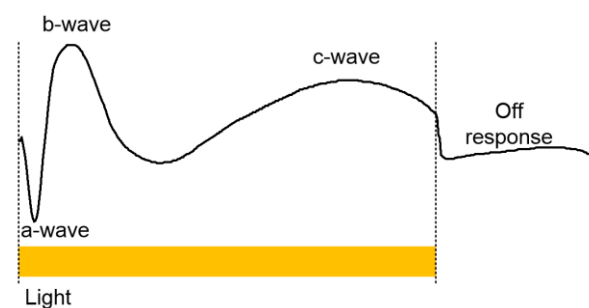
Fig. 1.3 Typical ERG with long stimulation showing major ERG components. Reprinted from [40] with permission.

Figure 1.3 shows typical ERG with a relatively long stimulation. The main components of ERG, a-wave, b-wave, c-wave and off response (d wave), are shown. Off response can only be observed with long stimulation (>100 ms). ERG a-wave is generated by photoreceptors. It is a

result of hyperpolarization of photoreceptor outer segment (OS) [41, 42]. Photons initiate phototransduction process in photoreceptor OS and ultimately lead the sodium ion channels to close, reducing the influx of sodium ions, and the photoreceptor hyperpolarizes and a-wave is generated. When the photoreceptor is hyperpolarized, neurotransmitter release is reduced, then post synaptic bipolar cells are depolarized. The depolarization of bipolar cells increases extracellular potassium concentration in OPL [43, 44]. Extracellular potassium concentration in IPL also increases because of light-induced activity of amacrine and ganglion cells [43-45], and extracellular potassium concentration in photoreceptor layer decreases due to photoreceptor hyperpolarization. The changes of potassium concentration in OPL, IPL, and photoreceptor layers alter Müller cell membrane potential and generate current across Müller cell. The current causes Müller cells to depolarize and generate the ERG b-wave [46, 47]. The ERG c-wave is generated from RPE cells. The decrease in extracellular potassium concentration in photoreceptor layer interrupts the established extracellular potassium concentration difference between the retina and the choroid, and results in a change in the whole trans-epithelial potential, which is recorded as c-wave [48, 49].

1.1.4 Optical coherence tomography

Besides ERG, another standard diagnosing tool in eye clinic is OCT. OCT is an imaging modality that achieves high axial resolution by coherence gating [50]. Because of the high axial resolution, it provides detailed information of the layered structure of the retina, which is useful in diagnosing retinal diseases like AMD [51, 52] and RP [53, 54]. There are different modalities of OCT, i.e. time domain OCT (TD-OCT), SD-OCT, and swept source OCT [55, 56]. TD-OCT and SD-OCT were used in this dissertation research.
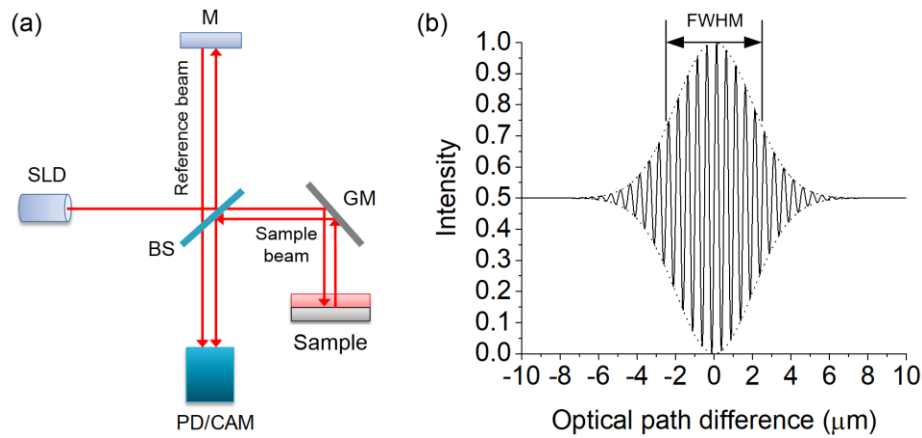
Fig. 1.4 Working principle of OCT. (a) Diagram showing the basic light path of an OCT. SLD: superluminescent diode; M: mirror; BS: beam splitter; GM: galvo mirror; PD/CAM: photodiode or camera. (b) Typical interference intensity curve acquired when moving the reference mirror. FWHM: full width half maximum.

Fig. 1.4(a) illustrates the setup of an OCT. The light source of TD-OCT and SD-OCT is low coherence light generated by the superluminescent diode (SLD). Low coherence means the coherence length is short (e.g. several micrometers), i.e., when optical path difference of the two interference beams increases, the coherence intensity will rapidly decrease, as shown in Fig. 1.4(b). As shown in Fig. 1.4(a), light from SLD is split into two beams, the reference beam and the sample beam. Light in reference beam is reflected by a mirror and goes to the camera. Light in sample beam is reflected by the sample and also goes to the camera. Due to the complex structure of the sample, light is reflected from different depths of the sample. Thus light reflected from the sample has different optical path lengths. Light reflected from mirror and sample interferes with each other on camera sensor plane. Due to the low coherence length of the light source, light reflected from the mirror will only interfere with light reflected from the sample that has very close optical path length as light reflected from the mirror. In other words, the interference will occur only between light reflected from mirror and light reflected from a certain depth of the sample. Thus, image from that certain depth of the sample could be acquired. In TD-OCT, the image of different depth is acquired by moving the reference mirror or

the sample. In SD-OCT, both mirror and sample are fixed and depth information is carried by the spectrum of interfering light.

Same as wide-field microscope, the lateral resolution of OCT is determined by the objective numerical aperture (NA)

$$r_{x,y} = \frac{0.61\lambda}{NA} \qquad (1.1)$$

Axial resolution is determined by the coherence length of the light source, and is defined as the full width half maximum (FWHM), as shown in Fig. 1.4(b)

$$r_z = \frac{2\ln 2}{\pi} \frac{\lambda_0^2}{\Delta\lambda} \approx 0.44 \frac{\lambda_0^2}{\Delta\lambda} \qquad (1.2)$$

Where λ_0 is the central wavelength of the light source, $\Delta\lambda$ is the bandwidth of the light source.

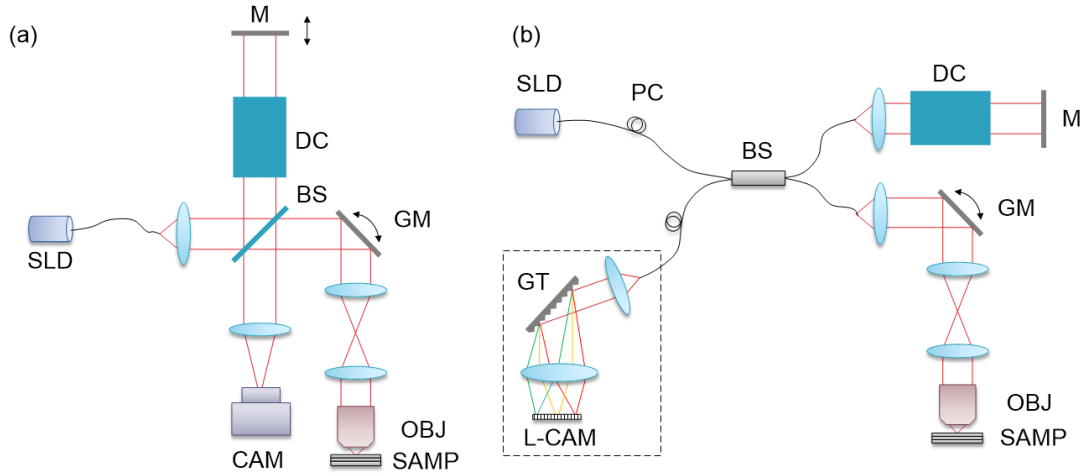Fig. 1.5 Typical optical setup of TD-OCT and SD-OCT. (a) Optical setup of TD-OCT. SLD: superluminescent diode; M: mirror; DC: dispersion compensation component; BS: beam splitter; GM: galvo mirror; OBJ: objective; SAMP: sample; CAM: camera or photodiode. (b) Optical setup of SD-OCT. The dashed line rectangle shows the spectrometer. PC: polarization controller; GT: grating; L-CAM: linear camera.

Figure 1.5(a) shows the typical optical setup of a TD-OCT. In TD-OCT, light coming out of SLD is split by beam splitter. One beam goes to the mirror and then is reflected back to the camera. The other beam is scanned by a galvo mirror, passes a pair of lenses and is focused onto the sample by an objective. The galvo mirror and objective entrance pupil are conjugate so that light could always go through objective entrance pupil despite the scanning angle of the galvo mirror. Thus, vignette effect is avoided. Light reflected from the sample is reflected to camera by the galvo mirror and the beam splitter and interferes with light reflected from the mirror. A linear camera is used when the system is in line-scan configuration, i.e., a scanning line is formed on the sample for illumination. If the system is point scanning OCT, the camera could be replaced with a single element light detector, e.g. photodiode.

Figure 1.5(b) shows the typical optical setup of a SD-OCT. The sample beam and reference beam are the same as in TD-OCT. One difference between the setups of TD-OCT and SD-OCT is that fiber based beam splitter is used in SD-OCT, instead of free space beam splitter as in TD-OCT. That is because SD-OCT uses point scanning configuration, free space beam splitter is not necessary for SD-OCT and fiber based beam splitter could simplify the system setup. The other, also most important difference is, a spectrometer is used to record the spectrum of interfering light instead of a camera that records only intensity information. Depth information of the corresponding scanning position is carried in the frequency information of the spectrum. After doing Fourier Transformation of the spectrum, the A-scan (depth information) is acquired. As the galvo mirror scans the sample, multiple A-scans could be acquired and forms a B-scan, which shows the cross-section of the sample.

1.1.5 Intrinsic optical signal

Even though ERG and OCT are widely used in retinal diseases diagnosis, they both have their limitations. Because ERG measures integrated electrical signal of the retina, it lacks spatial

resolving capability. OCT has a high spatial resolution but could only detect the diseases after morphological changes show up. A new tool that is capable of early detection of retinal disease and provides high resolution retinal images is desirable. Intrinsic optical signal (IOS) [57] is a promising option.

IOS reflects the intrinsic optical property changes of the retina after being stimulated by light. The optical property changes could include changes in reflectance, scattering, birefringence, and polarization, etc. These changes are observed as pixel intensity changes in recorded images. The percentage of pixel intensity change compared to pixel intensity before stimulation is the IOS. IOS is often denoted as ΔI/I, where ΔI is the pixel intensity change and I is the pixel intensity before stimulation. To calculate ΔI/I, images before and after stimulation need to be acquired. Different imaging modalities could be used for IOS imaging, including full-field microscopy, confocal microscopy and OCT, etc.

To do IOS imaging, first, images before and after light stimulation are acquired continuously at a certain frame speed. At a certain time point, a visible light stimulation of certain intensity and duration is delivered to the retina. Acquired images are processed to get IOS images. To get IOS images from recorded images, first, pre-stimulus images are averaged and served as baseline image $I_0(x,y)$. Then each image is calculated to get corresponding IOS image using the equation:

$$IOS_t(x,y) = \frac{I_t(x,y) - I_0(x,y)}{I_0(x,y)}$$

(1.3)

Where $IOS_t(x,y)$ is the IOS image at time t. $I_t(x,y)$ is the original image at time t. Multiple IOS images could be averaged to increase the signal to noise ratio (SNR) of IOS.

To calculate IOS curves, the 3-σ standard was applied to select active pixels. First, pre-stimulus images are used to calculate the standard deviation of each pixel, σ(x,y). Then for each pixel in

each image, if the pixel intensity is greater than $I_0+3\sigma$, the pixel is a positive pixel, if the pixel intensity is smaller than $I_0-3\sigma$, the pixel is a negative pixel. To reduce the possibility that an inactive pixel is classified as positive or negative pixels, the pixel is classified positive or negative pixel only if it meets the 3-σ standard in 5 consecutive images. To calculate positive and negative IOS curves, all positive pixels in each image were averaged and all negative pixels in each image were also averaged, and we get two intensity curves of positive and negative pixels. Then IOS curves are calculated as:

$$IOS(t) = \frac{I(t) - I_0}{I_0}$$

(1.4)

Where I_t is the value of the intensity curves at time t, and I_0 is the pre-stimulus average of the intensity curves.

Different IOS parameters including onset time, amplitude and time-to-half-peak were calculated from IOS curves and used in this dissertation research for quantifying retinal function. To calculate onset time,

Figure 1.6 shows typical IOS images and curves acquired from frog retina using SD-OCT. Figure 1.6(a1) shows the IOS images at different times under 10 ms stimulation and Fig. 1.6(a2) shows IOS images under 500 ms stimulation. We could see that with short stimulation (10 ms), IOS is mainly observed in OS and with long stimulation (500 ms) IOS is observed in both OS and IPL. Figure 1.6(b) shows active pixels at different time with 10 ms stimulation and Fig. 1.6(c) shows active pixels with 500 ms stimulation. With both short and long stimulation, active pixels were observed in OS. Only with long stimulation, active pixels slowly appeared in IPL. Figure 1.6(d) and (e) show IOS curves from different retinal layers with 10 ms and 500 ms stimulation. With 10 ms stimulation, IOS was mainly observed from inner segment ellipsoid (ISe), OS and RPE. However, with 500 ms stimulation IOS is observed also in IPL and OPL. Fast IOS from

OS and RPE reaches the peak in very short time (millisecond level) while slow IOS from IPL and OPL has slow rising phase (second level).
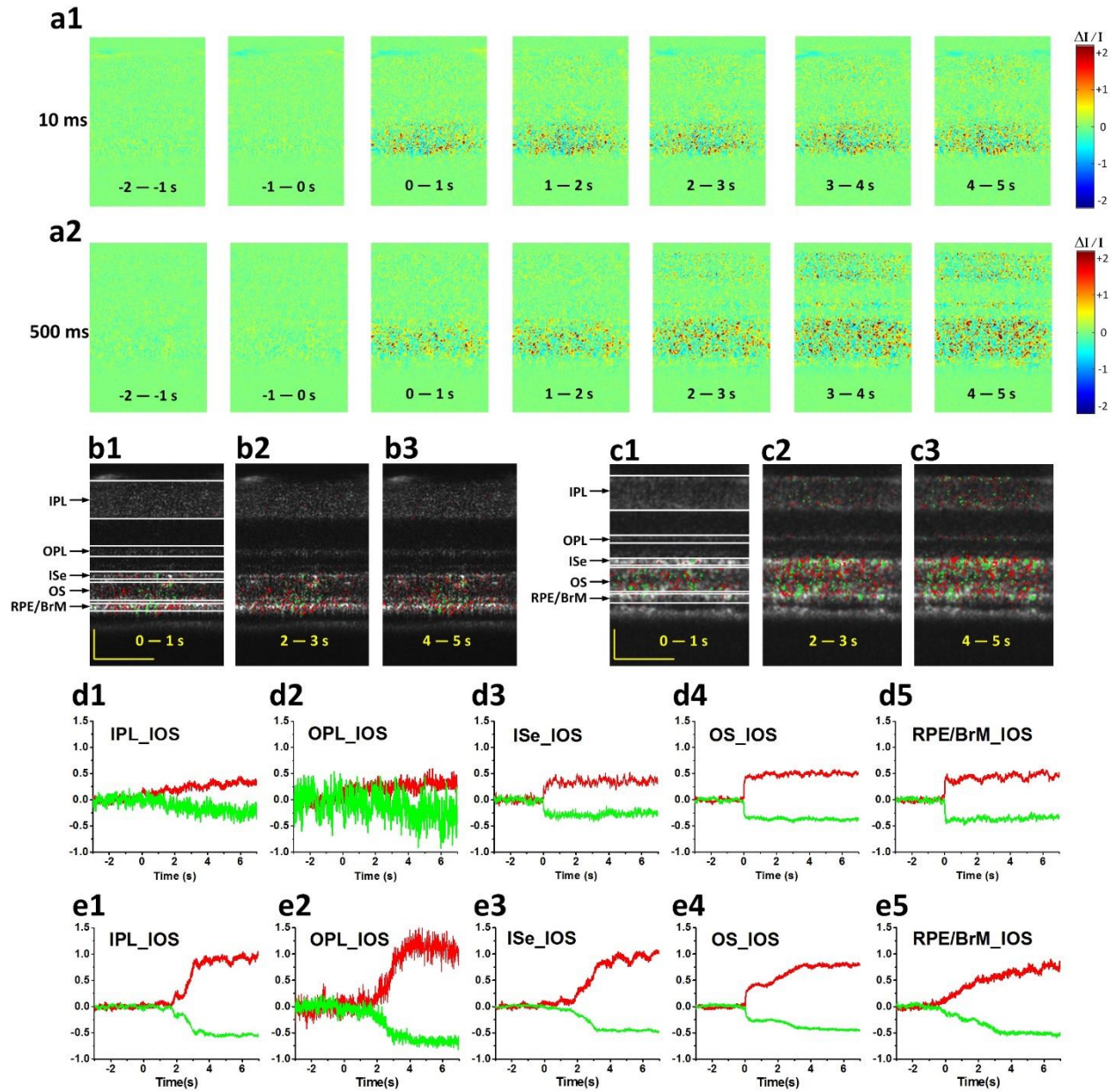
Fig. 1.6 Representative IOS from OCT images. (a1) IOS images with 10 ms stimulation; (a2) IOS images with 500 ms stimulation; (b) IOS map of 10 ms stimulation superimposed on OCT image; Red show positive pixels and green show negative pixels. (c) IOS map of 500 ms stimulation superimposed on OCT image. Red show positive pixels and green show negative pixels. (d) IOS curves from different retinal layers with 10 ms stimulation. (e) IOS curves from different layers with 500 ms stimulation. Reprinted from [16] with permission.

The mechanism of IOS is not fully understood yet. Anatomically, fast IOS is observed mainly in ISe, OS and RPE, and slow IOS is observed mainly in IPL and OPL [16]. Physiologically, IOS is a result of complex activities in the stimulated retina. Any response of the retina that could result in optical property changes will be recorded as IOS. For example, the phototransduction process, which includes the transformation of proteins and closure of ion channels, could result in scattering light changes [58]. Besides stimulus-evoked neural activities, subsequent metabolic and hemodynamic changes could also result in observed light intensity changes. When the retina is stimulated, the activity of retina results in increased requirement of energy and oxygen, thus blood supply to the retina will increase and such change could be recorded as slow IOS [59].

1.2 Overview of the dissertation research

Many studies have been conducted regarding IOS characteristics and properties on animal models including frogs [1, 12-16, 60-63], chickens [64, 65], rats [66], rabbits [67], cats [68] and primates [69]. Studies on humans were also reported [70-72]. Studies using microscopy and custom designed imaging systems, including confocal microscopy and OCT, showed that in frogs, fast IOS mainly originated from photoreceptor outer segments [16]. In a study using *in vivo* confocal microscopy, we demonstrated the capability of IOS in retinal dysfunction detection. The frog retina was injured with a high-power laser, no obvious morphological changes could be observed from the confocal image of the retina while fast IOS accurately showed the injured area [14]. In another study, with isolated retinas from rod degenerated mutant mice, we observed significantly smaller stimulus evoked IOS in 2-month-old mouse, while no stimulus evoked IOS was observed in 1-year old mouse [73]. Those studies confirmed the feasibility of using IOS as a tool for mapping retinal function and promised the possibility of using IOS to diagnose retinal diseases clinically. However, our understanding about IOS is still limited regarding its characteristics, mechanism and relationship with retinal disease. There is a long

way to go before clinical application of IOS. This dissertation research is designed to systematically study the characteristics of IOS and understand how IOS is affected by retinal diseases, so as to push clinical application of IOS one step further.

1.2.1 Significance

IOS imaging as a potential diagnosing tool is superior to currently available approaches in two aspects combined, functional imaging and high resolution. Most diagnosing tools in clinic are either functional evaluating tools, e.g. ERG, with low spatial resolution, or morphological imaging tools, e.g. OCT, that are not capable of early detection of diseases. IOS is a new tool that is capable of functional imaging of the retina with high resolution. Function imaging makes IOS a great tool for diagnosing retinal dysfunction in early stages to help increase the possibility of a complete cure and reduce the expenses of treatment. High resolution makes IOS possible to accurately determine the location of degenerated cells, thus making the diagnosing process much easier and less subjective compared to other diagnosing tools such as visual field test. With the benefit of high resolution functional imaging capability, early diagnosis of different retinal diseases is made simpler.

Before applying IOS in clinic, it is important to improve our knowledge about IOS. In this dissertation research, characteristics of IOS were systematically studied, mechanism of fast IOS was explored, and the relationship between fast IOS and retinal diseases was quantified. The feasibility of using fast IOS as a tool for diagnosing retinal diseases in small animal models was tested and proven. This study paved the way for further IOS studies in different animal models and humans. The results suggest that IOS could be a novel high resolution functional imaging tool for retinal disease diagnosis.

1.2.2 Innovation

Although IOS imaging has been conducted in both isolated [1, 13, 60, 63, 73] and intact retinas [16, 64, 66, 69, 70], IOS study in diseased mouse models is difficult because of the small mouse eye and eye movement. The bridge that connects lab study and clinical application is not built yet. The innovation of this dissertation research is, systematically designed studies were conducted to better understand IOS and to push IOS imaging one step closer to clinical application. By building specially designed imaging systems, characteristics of normal IOS was carefully studied, the mechanism of fast IOS was explored and fast IOS in a diseased mouse model was studied. These studies paved way for using IOS as a diagnosing tool in clinic.

First, characters of normal IOS were systematically studied. Using a LS-OCT, fast IOS from OS of frog retina was selectively imaged to study fast IOS distribution and time course. Using an *in vivo* SD-OCT, IOS from both outer and inner retina of living mouse was investigated. The response of fast IOS to stimulation intensity was studied. These studies provided details of characteristics of IOS.

Second, both dynamical and physiological mechanisms of fast IOS were explored. Using a system that combines line-scan confocal microscopy and SD-OCT, phototropism was observed to be one main dynamical origination of fast IOS. In the *in vivo* study using mouse retina, by comparing fast IOS time course with ERG time course, we proposed that early phototransduction process might be the physiological origination of fast IOS.

Third, fast IOS imaging in a diseased mouse model was conducted to study diseases introduced fast IOS distortion. The feasibility of fast IOS in diagnosing retinal disease was demonstrated. This built the foundation for clinical application of IOS.

1.2.3 Specific Aims

The overall goal of this proposal is to study the characteristics of IOS, understand its mechanism, and explore the feasibility of utilizing IOS as a tool for diagnosing retinal diseases.

Aim 1: Observing normal IOS and studying how stimulation affects IOS. Knowing the characteristics of normal IOS is the foundation of IOS imaging. Only when we fully understand what normal IOS is like with different stimulation, disease introduced IOS distortion could be interpreted.

Aim 2: Exploring the mechanism of fast IOS. Without knowing the mechanism behind fast IOS, it is difficult to put fast IOS into application. Understanding the mechanism could help explain how fast IOS is affected by stimulation and retinal diseases, thus proper protocol could be developed for conducting fast IOS imaging both in research and in clinic.

Aim 3: Studying the relationship between retinal dysfunction and IOS distortion. This aim is designed to study how fast IOS changes as retinal degeneration progresses and study how fast IOS of mutant mice is different from fast IOS of wild type mice. The study will correlate degeneration stages with fast IOS changes and thus will prove the feasibility of using fast IOS to diagnose and track retinal diseases.

1.2.4 Structure of the dissertation

Four studies were designed and conducted in this dissertation research. While each study focuses on one aspect of IOS, it also revealed information on other aspects. All studies are not totally independent and have some interlaces.

The study in Chapter II was designed to understand the normal fast IOS from OS. It is known that OS is one main anatomical origination of fast IOS [15, 63]. Fast IOS from OS of frog retina was explored using a LS-OCT. Results showed that positive and negative fast IOSs were mixed

and confined in the stimulated area. Time course of fast IOS from OS was very fast, both positive and negative fast IOSs reaches half-peak in <10 ms. However, negative fast IOS is slightly faster than positive fast IOS, suggesting that negative and positive fast IOSs originated from different processes. We suspected that fast IOS reflect dynamics of G-protein binding and releasing in early phases of phototransduction.

After studying the characteristics of normal IOS, Chapter III focused on exploring the dynamical mechanism of fast IOS. Using a wide-field microscope, rod phototropism was observed in a previous study [74]. Phototropism was further explored in Chapter III to see if it could be the origination of fast IOS. Results indicate that phototropism occurred in OS, thus it acted as the main contributor to fast IOS observed in OS.

Before pursuing clinical application of IOS, it is necessary to study how different diseases alter IOS. Chapter IV focused on building the foundation for *in vivo* IOS imaging in mice so that IOS from different diseased mouse models could be studied. IOS from normal mice was explored. The response of fast IOS to different stimulation conditions was compared to that of ERG. Results showed that the response of fast IOS to stimulation intensity was very similar to the response of ERG a-wave, indicating that same as ERG a-wave, fast IOS also originated from phototransduction process. However, the onset time of fast IOS was significantly shorter than that of ERG a-wave, thus fast IOS probably originated from the early phases of phototransduction. This agrees with the hypothesis made in Chapter II.

With the foundation of IOS imaging in mice built, Chapter V studied disease introduced fast IOS distortion using mouse pups of a retinal degeneration model. Results showed that fast IOS and OCT could detect retinal degeneration at 16 and 17 days after birth, respectively. The results proved that fast IOS could detect retinal dysfunction before morphological changes could be observed. In other words, fast IOS was capable of early detection of retinal diseases.

Chapter VI summarized the results of the studies, and discussed future directions of IOS study and challenges of IOS in clinical application.

CHAPTER II. *EN FACE* OPTICAL COHERENCE TOMOGRAPHY OF FAST LIGHT RESPONSE AT PHOTORECEPTOR OUTER SEGMENTS IN LIVING FROG EYECUP

Abstract: This study was designed to test the feasibility of *en face* mapping of the fast intrinsic optical signal (IOS) response at photoreceptor outer segments and to assess the effect of spatial resolution on functional IOS imaging of retinal photoreceptors. A line-scan optical coherence tomography (LS-OCT) was constructed to achieve depth resolved functional IOS imaging of living frog eyecups. Rapid *en face* OCT revealed fast IOS almost immediately (<3 ms) after the onset of visible light flashes at photoreceptor outer segments. Quantitative analysis indicated that the IOS kinetics may reflect dynamics of G-protein binding and releasing in early phases of visual transduction, and high resolution is essential to differentiate positive and negative IOS changes in adjacent locations.

2.1 Introduction

Eye diseases, such as age-related macular degeneration (AMD) [4] and retinitis pigmentosa (RP) [6] can cause pathological changes in retinal photoreceptors. Without prompt and effective intervention, they can ultimately lead to severe vision losses and even legal blindness. High resolution imaging tools provide important information for retinal diseases diagnosis and treatment evaluation. Advanced fundus examinations, including optical coherence tomography (OCT) and adaptive optics (AO) measurements, have provided valuable information for AMD assessment. However, the morphological only fundus examination is not enough [75]. Electroretinogram (ERG) [11], focal ERG, multifocal ERG [19], perimetry [76], etc. are widely used for objective retinal function evaluation. However, due to the low spatial resolution of ERG

and perimetry, they are not suitable for precisely identifying localized retinal dysfunctions. At early stages, AMD associated cellular damages are in the form of degenerative or apoptotic changes of small groups of retinal cells. Although morphological (e.g. OCT) and functional (e.g. ERG) evaluation methods could be combined [77] to provide more comprehensive information for retinal disease evaluation, conducting these separate measurements is time-consuming and cost inefficient. Moreover, the loci of functional ERG losses may not correlate with those of the discernible morphological features, such as drusen, hemorrhages, etc. [78, 79]. It is therefore desirable to be able to simultaneously evaluate structure and function of individual retinal layers at high spatial and temporal resolution over an extended retinal region.

Intrinsic optical signal (IOS) imaging derives functional information of the retina from high resolution morphological images, thus it promises a new method for high resolution functional mapping of the retina. Stimulus-evoked IOSs have been detected in the retina, neural tissues [80-83] and other excitable cells [84, 85]. Several imaging techniques, including fundus cameras [69, 86], AO ophthalmoscopes [87-89], OCT imagers [66, 67, 90] have been explored for functional IOS imaging of the retina. While all these studies have revealed robust IOSs associated with retinal stimulation, rapid *en face* mapping of fast IOS selectively from retinal photoreceptors over an extended area, which is essential for easy photoreceptor assessment, is still challenging due to crosstalk noises among multiple retinal layers. Recently, we developed a line-scan confocal imager to detect fast IOS tightly correlated with photoreceptor response [12, 14]. However, the axial resolution of the confocal system was limited, and sub-cellular correlate of the IOS in retinal photoreceptor has not been well understood. Dynamic near infrared (NIR) microscopy of retinal slices, which opened a cross section of retinal layers, disclosed a dominant IOS source at photoreceptor outer segments. In this Letter, we report depth-resolved *en face* OCT imaging of IOS response at photoreceptor outer segments in living frog eyecups at sub-cellular resolution.

2.2 Methods

Eyecups of leopard frogs (Rana Pipiens) were selected for this study. Protocols for all experiment procedures were approved by the Institutional Animal Care and Use Committee of the University of Alabama at Birmingham. During the experiment, the frog was first dark adapted for ~2 h and then euthanized by rapid decapitation and double pithing. Eyeballs were then dissected and moved to Ringer's solution (containing in mMol/L: 110 NaCl, 2.5 KCl, 1.6 MgCl$_2$, 1.0 CaCl$_2$, 22 NaHCO$_3$, and 10 D-glucose). The eyecup was made by hemisecting the eye globe below the equator with fine scissors and then removing the lens. Surgical operation was conducted in a dark room illuminated with dim red light. The eyecup was immersed in Ringer's solution during functional IOS imaging of retinal response.
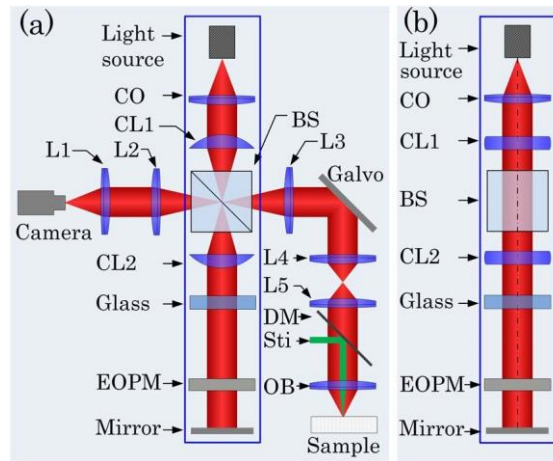
Fig. 2.1. Schematic diagram of the time domain LS-OCT. (a) Top view of the system. CO, collimator; L1–L5, lenses, with focal lengths 80, 40, 80, 40, and 75 mm, respectively; OB, objective (10✕, NA=0.3); CL1 and CL2, cylindrical lenses, with focal lengths 75 mm; BS, beam splitter; DM, dichroic mirror; Sti, green light stimulus; EOPM, electro-optic phase modulator. (b) Side view of blue rectangle area in (a).

In order to conduct *sub-cellular* resolution *en face* IOS imaging of the retina, a rapid time domain line-scan OCT (LS-OCT) system was developed. The LS-OCT combined technical merits of electro-optic phase modulator (EOPM) modulation and line-scan strategy to achieve rapid, vibration-free OCT imaging [91]. Figure 2.1 shows a block diagram of the time domain

LS-OCT system. A NIR superluminescent diode (SLD-351, Superlum), with center wavelength λ=830 nm and bandwidth Δλ=60 nm, was used for dynamic OCT imaging. In the illumination path, the cylindrical lens CL1 was used to condense the NIR light in one dimension to produce a focused line illumination at the retina. The focused line illumination was scanned over the retina by a galvo (GVS001, Thorlabs) to achieve rapid *en face* imaging. In the reference path, the cylindrical lens CL2 was used to convert the focused light back to collimated light. The glass block was used to compensate for optical dispersion. The EOPM (Model 350-50, Conoptics) was used to implement vibration-free phase modulation. Light reflected by the mirror and the retina interfered and was captured by the line-scan camera (Sprint spl2048-140km, Basler) to retrieve OCT images [91]. The line-scan camera had line speed up to 140,000 lines/s when working at double-line mode and 70,000 lines/s at single-line mode. Single-line mode was selected for this study to ensure high resolution of IOS recording. In coordination with the NIR line illumination, the 1D CMOS array (1×2048 pixels, 10μm×10μm) of the line-scan camera acted as a slit to achieve a confocal configuration for effective rejection of out-of-focus light.

2.3 Results

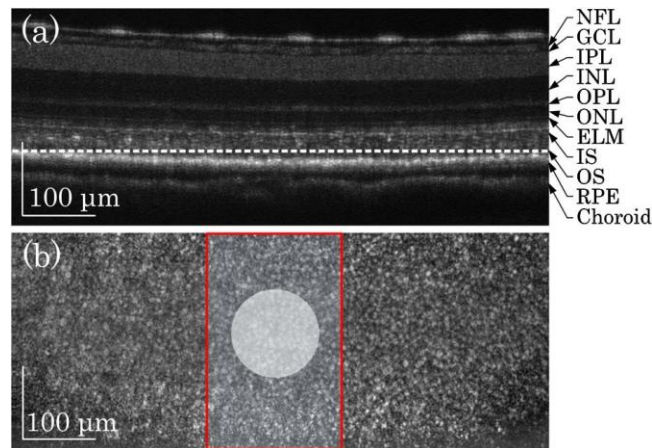Fig. 2.2. LS-OCT images of frog eyecup. (a) OCT B-scan image. The image revealed multiple hyper-reflective OCT bands, including NFL, GCL, IPL, INL, OPL, ONL, ELM, IS, OS, RPE, and choroid. (b) Representative *en face* OCT image recorded at photoreceptor OS [indicated by the dashed white line in (a)]. The red rectangle area shows the area where IOS images were acquired. The white spot indicates the green light stimulus.

Using a 10× (NA=0.3) water immersion objective, lateral and axial resolutions of the system were ~2 µm (0.61λ/NA) and ~4 µm (0.44λ^2/nΔλ, where n was refractive index of retinal tissue, n ≈1.4), respectively. Figure 2.2 shows representative time domain LS-OCT images of living frog eyecups. The B-scan OCT [Fig. 2.2(a)], which revealed a cross-sectional image of the eyecup, was reconstructed from a stack of *en face* OCT images acquired at 50 frames per second (fps). Figure 2.2(a) disclosed clear structures of outer segment (OS), inner segment (IS) ellipsoid, external limiting membrane (ELM), outer plexiform layer (OPL), inner nuclear layer (INL), inner plexiform layer (IPL), ganglion cell layer (GCL), and nerve fiber layer (NFL). In the *en face* OCT image [Fig. 2.2(b)], individual photoreceptors could be unambiguously identified.

Given excellent axial resolution, we focused the OCT recording at photoreceptor outer segments [dashed white line in Fig. 2.2(a)]. For better temporal resolution, we reduced the field of view [Fig. 2.2(b) red rectangle area] and increased frame speed from 50 to 200 fps. The details of IOS processing procedure have been documented in our previous publication [14]. Briefly, IOS images are illustrated with a unit of ΔI/I, where I is the background obtained by averaging pre-stimulus images, and ΔI is the difference between each image and the background. Figure 2.3(a) illustrates IOS images of photoreceptor outer segments. A green light flash [white spot in Fig. 2.3(a2)] was introduced for photoreceptor stimulation at time 0. In Fig. 2.3(a), it was observed that the IOS pattern showed a tight correlation with the stimulus spot. In other words, the IOS response was predominantly confined to the stimulus spot. Positive and negative IOSs were observed in the stimulus-activated area. Figure 2.3(b) shows separate averages of positive and negative IOSs in the image area. Positive and negative signals were defined by the 3−δ rule [14].
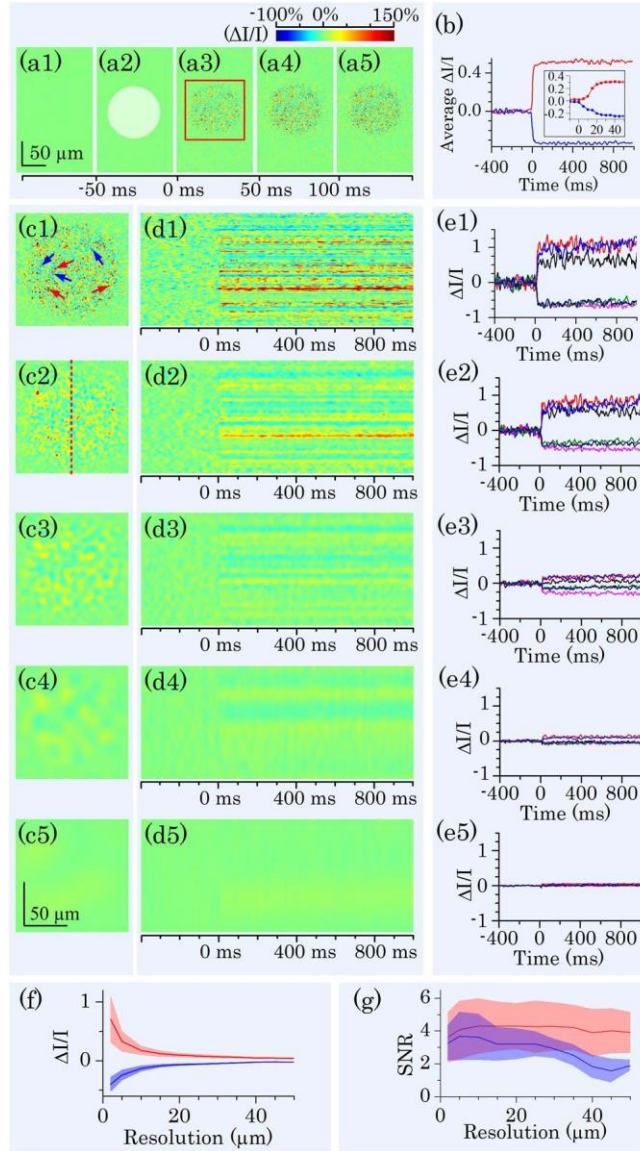
Fig. 2.3. IOS images and curves acquired at 200 fps. (a) Representative IOS images, with a time interval of 50 ms. A 10 ms green light stimulus was introduced at time 0 (a2). Rapid IOS occurred immediately after the stimulation; mixed positive and negative IOSs were observed. (b) Separate averages of positive (red trace) and negative (blue trace) IOSs. The inset is enlarged curve of early IOS response. (c) IOS images with computationally controlled resolutions. Resolutions in (c1) to (c5) were 2, 5, 10, 20, and 50 µm, respectively. (d) Spatiotemporal IOS pattern at the position marked by the red dashed line in (c2). (e) Temporal IOS profiles of representative pixels marked by arrows in (c1). Red arrows indicated positive IOS pixels; blue arrows indicated negative IOS pixels. (f) The relationship between resolution and IOS magnitudes of representative pixels within stimulated area. Red curves represent positive IOS; blue curves represent negative IOS. Shadow areas show standard deviation. (g) The effect of resolution on IOS SNR. Red curves represent positive IOS; blue curves represent negative IOS. Shadow areas show standard deviation.

The mixed positive and negative IOSs indicated that high resolution was essential for IOS sensitivity of IOS imaging. Otherwise, IOSs with different signal polarities could integrate together to lower IOS magnitude. Figure 2.3(c) illustrates quantitative assessment of the effect of spatial resolution on IOS measurement. Variable resolutions were computationally implemented by applying different sized Butterworth windows in Fourier domain to OCT images. Figure 2.3(e) shows IOS curves of representative positive [red arrows in Fig. 2.3(c1)] and negative [blue arrows in Fig. 2.3(c1)] pixels at different resolutions. It was observed that the IOS magnitude dropped as the resolution decreased. At 50 µm resolution, IOS patterns could be barely observed. Figure 2.3(f) shows separate average of positive and negative IOSs observed in Fig. 2.3(a). Both positive and negative IOSs decreased rapidly with lowered resolution. Figure 2.3(g) illustrates the effect of spatial resolution on IOS signal-to-noise ratio (SNR). In comparison with significant effect of the resolution on IOS magnitude, the effect on IOS SNR was relatively insignificant.
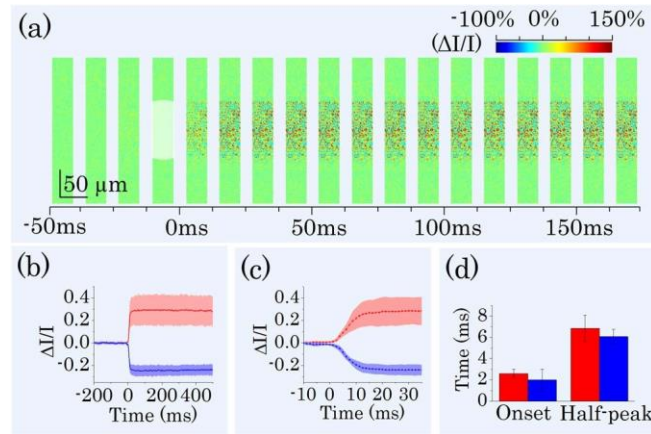
Fig. 2.4. IOS images and curves acquired at 800 fps. (a) A sequence of IOS images. Image width is one quarter of image width in Fig. 2.3(a). Time interval of presented images is 12.5 ms. A 10 ms green light stimulus was introduced at time 0. (b) Separate averages of positive and negative IOSs. Red curves represent positive IOS; blue curves represent negative IOS. Shadow areas show standard deviations. (c) Enlarged image of (b) from −10 to 35 ms. (d) Onset time and half-peak time of average IOSs of nine different recordings. Red bars represent positive IOS; blue bars represent negative IOS.

As shown in Fig. 2.3(b), the IOS response occurred almost immediately and reached half-peak and maximum at ~10 and ~30 ms, respectively. Slight difference of the onset times of positive and negative IOSs was observed in the inset panel of Fig. 2.3(b). In order to investigate the onset time courses of positive and negative IOSs, we improved imaging speed from 200 to 800 fps. Figure 2.4(a) shows representative IOS images recorded at 800 fps. Figure 2.4(b) shows averaged IOS curves of nine recordings. Here we defined onset time as the time that IOS magnitude reached $\mu+3\sigma$, where μ and σ were mean and standard deviation of pre-stimulus IOS of each pixel. From Fig. 2.4(c) we could estimate that onset time was within 3 ms and half-peak time was within 10 ms. Figure 2.4(d) shows mean values of onset time and half peak time of positive and negative IOSs calculated from curves in Fig. 2.4(b). For positive IOS, the mean onset time was 2.5 ms, and the mean half-peak time was 7 ms; for negative IOS, the mean onset time was 2 ms, and the mean half-peak time was 6 ms. Mean temporal parameter values of negative IOS were smaller than that of positive IOS. We conducted one-tailed unpaired Student's *t*-test for those data. At 10% level of significance, we could say that negative IOS onset time was shorter than that of positive IOS and negative IOS half-peak time was shorter than that of positive IOS (*p*-values were 0.08 and 0.07 for onset time and half-peak time, respectively).

2.4 Discussion

In summary, a LS-OCT system was developed to conduct sub-cellular resolution IOS imaging of retinal photoreceptors in a living eyecup. High axial resolution enabled us to conduct selective IOS mapping of photoreceptor outer segments. High-resolution images revealed a robust IOS pattern, with mixed positive and negative responses in adjacent locations. Computational simulation indicated that high resolution was essential to ensure high IOS sensitivity. However, the effect of spatial resolution on IOS SNR was relatively insignificant.

Interestingly, the best SNR was observed around 10 μm, which was slightly larger than the dimension of individual photoreceptors. We consistently observed that the onset time of positive IOS was slightly slower, compared to negative IOS [Figs. 2.3(b) and 2.4(d)]. This suggests that the observed positive and negative IOSs may reflect different aspects of light phototransduction in photoreceptors. Previous studies with isolated photoreceptor outer segments and isolated retinas have reported fast IOSs correlated with early procedures of visual phototransduction [92-94]. Both binding and releasing of G-proteins to photo-excited rhodopsin may contribute to the IOSs. While the early phase of negative IOS may be partially affected by the binding of photo-excited rhodopsin to G proteins, some part of the positive IOSs may relate to the dissociation of the complex upon GDP/GTP exchange [93]. Further investigation of spatiotemporal characteristics of the IOSs from photoreceptor outer segments is required to optimize instrument design for functional IOS imaging of retinal photoreceptors.

Acknowledgement

CHAPTER III. FUNCTIONAL OPTICAL COHERENCE TOMOGRAPHY REVEALS TRANSIENT PHOTOTROPIC CHANGE OF PHOTORECEPTOR OUTER SEGMENTS

Abstract: Dynamic near infrared microscopy has revealed transient retinal phototropism (TRP) correlated with oblique light stimulation. Here, by developing a hybrid confocal microscopy and optical coherence tomography (OCT), we tested sub-cellular source of the TRP in living frog retina. Dynamic confocal microscopy and OCT consistently revealed photoreceptor outer segments as the anatomic source of the TRP. Further investigation of the TRP can provide insights in better understanding of Stiles-Crawford effect (SCE) on rod and cone systems, and may also promise an intrinsic biomarker for early detection of eye diseases that can produce photoreceptor dysfunction.

3.1 Introduction

The Stiles-Crawford effect (SCE) refers to the directional sensitivity of the retina [95]. It is known that the retina is more sensitive to the light entering the center of the pupil, i.e., parallel light relative to eye axis, than the light passing through the periphery, i.e., oblique light illumination. The SCE is predominantly observed in cone photoreceptors, which is believed to suppress intraocular stray light to benefit image quality of photopic vision [96]. In contrast, psychophysical methods did not reveal significant SCE in rod photoreceptors that dominate scotopic vision [96]. The biophysical mechanism underlying the SCE difference between rod and cone photoreceptors is not well established. Recently, we observed transient retinal phototropism (TRP) correlated with oblique light stimulation, which might provide one possible explanation of

the lack of rod SCE. Using a near infrared (NIR) transmission microscope equipped with a high-speed camera, we have consistently observed the TRP in both amphibian (frog) and mammalian (mouse) retinas [74]. High spatial and temporal resolution imaging revealed that the TRP was rod-dominant. It has been widely accepted that the waveguide property of retinal photoreceptors can affect the directionality of light acceptance [97-99]. Therefore, such rod-dominant TRP might affect the waveguide acceptance and thus partially compensate for the loss of luminance efficiency in the rod system under oblique stimulation.

The purpose of this study is twofold: (1) to identify the axial location (e.g., inner or outer photoreceptor segment) of the TRP at micrometer resolution; and (2) to validate the feasibility of mapping TRP through reflected light imaging modality. The transmitted light microscopy in our preliminary study provided excellent transverse resolution to differentiate rod and cone photoreceptors [74]. However, limited axial resolution hampered its application to identify sub-cellular source and mechanism of the TRP. Moreover, transmitted light imaging modality limited its potential for *in vivo* application. In this study, we combined line-scan confocal microscopy and spectral-domain optical coherence tomography (SD-OCT) to demonstrate reflected light recording and characterize the sub-cellular source of the TRP in living frog retinas.

3.2 Methods

Figure 3.1 shows the schematic diagram of the confocal-OCT imaging system. In the line-scan confocal subsystem, a 780 nm superluminescent diode (QSDM-780-15D, Qphotonics) was used as the light source. A cylindrical lens was used to condense the light in one direction to produce a focused line illumination. Back reflection and scattering light from the sample was detected by a high-speed (70,000 lines/s) linear charge-coupled device (CCD) camera (AViiVA EM2, e2v). The linear CCD (1×1014 pixels, 10μm×10μm each pixel) naturally acted as a slit aperture, which was conjugated with the focused line illumination, to achieve confocal

configuration to reject out-of-focus light [1, 62, 100]. In the SD-OCT subsystem, an 850 nm SLD

(D840, Superlum) was used as the light source. The bandwidth of the near infrared SLD was

100 nm, corresponding to axial resolution ~3 μm in air. A 10× water immersion objective with

0.3 numeric aperture (NA) was employed to provide 1.7 μm lateral resolution. The SD-OCT and

line-scan confocal subsystems shared the same sample arm. A short-pass dichroic mirror DM1

(DMSP805, Thorlabs) was used to combine 780 and 850 nm light beams to achieve

simultaneous OCT and confocal imaging. A long-pass dichroic mirror DM2 (cut-on wavelength

700 nm, Edmund Optics) was used to introduce green light (505 nm) for retinal stimulation. The

stimulation orientation and TRP direction are defined in Figs. 3.2(A) and 3.2(B).
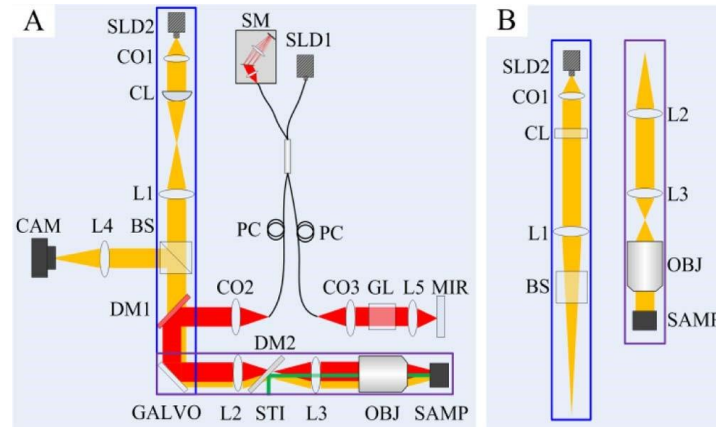
Fig. 3.1. Diagram of the hybrid confocal-OCT imaging system. (A) Top view: SLD1, superluminescent diode, λ=850 nm, Δλ=100 nm; SLD2, superluminescent diode, λ=780 nm, Δλ=50 nm; CO1–CO3, collimators; CL, cylindrical lens, f=150 mm; L1–L5, lenses, focal lengths are (in mm) 120, 60, 125, 160, and 30, respectively; BS, beam splitter; DM1, short-pass dichroic mirror; GALVO, galvo mirror; DM2, long-pass dichroic mirror; STI, stimulus light; OBJ, objective, 10×, NA=0.3; SAMP, sample; CAM, linear camera; GL, glass block; MIR, mirror; PC, polarization controller; SM, spectrometer. (B) Side view of blue and purple rectangle areas in (A). Only confocal part is illustrated.

Both amphibian (frog) and mammalian (mouse) retinas have previously been used to

demonstrate the TRP [74]. Freshly isolated leopard frog (Rana pipiens) retina was selected for

this study. Relative large photoreceptors (rods ~5−8 μm, cones ~1–3 μm) [101, 102] allowed

unambiguous observation of photoreceptor mosaic, and thus to readily enable quantitative

analysis of the TRP at sub-cellular resolution. Animal handling was approved by the Institutional

Animal Care and Use Committee of the University of Alabama at Birmingham. During the experiment, the frog was euthanized by decapitation followed by double pithing. The eyeball was then dissected and transferred to Ringer's solution (containing in mMol/L: 110 NaCl, 2.5 KCl, 1.6 $MgCl_2$, 1.0 $CaCl_2$, 22 $NaHCO_3$, and 10 D-glucose) [103]. After hemisecting the eyeball, the retina was isolated and moved to a chamber filled with Ringer's solution for imaging. The whole process was conducted in a dark room with dim red-light illumination.
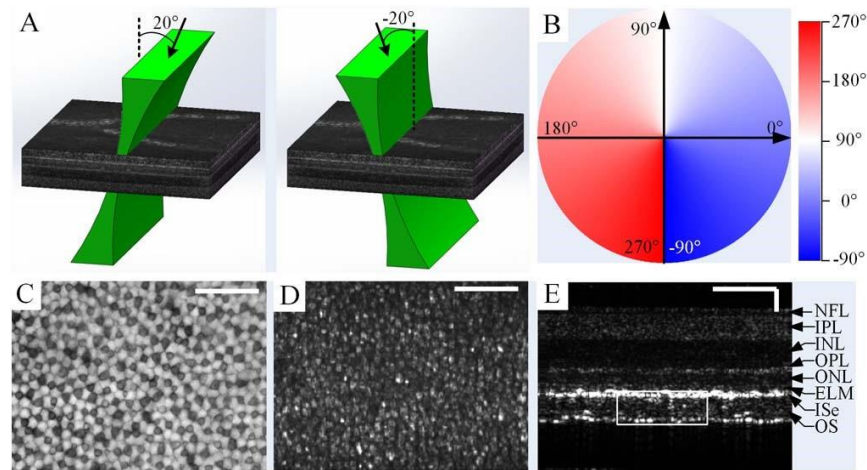
Fig. 3.2 (A) Illustration of 20° (left) and -20° (right) oblique stimulations. (B) Color code of TRP direction. (C) Frog photoreceptor mosaic pattern acquired with a NIR transmission microscope. (D) Frog photoreceptor mosaic pattern acquired with the line-scan confocal microscope. (E) A representative frame of the OCT movie (see Media 1). Dynamic OCT imaging revealed TRP in the area (white window) activated by the oblique stimulation. NFL, nerve fiber layer; IPL, inner plexiform layer; INL, inner nuclear layer; OPL, outer plexiform layer; ONL, outer nuclear layer; ELM, external limiting membrane; ISE, inner segment ellipsoid; OS, outer segment. Scale bars: 50 µm.

3.3 Results

In our preliminary study of TRP, we observed clear photoreceptor mosaic pattern in NIR transmission microscopy image, and rods and cones could be directly differentiated [Fig. 3.2(C), white cells: rods, black cells: cones]. In this study, photoreceptor mosaic pattern was also unambiguously observed in *en face* confocal image [Fig. 3.2(D)], although it was difficult to differentiate rod and cone cell types in the reflected light images. The integrated OCT provided cross-sectional observation of retinal structure at micrometer resolution [Fig. 3.2(E)]. The

combined confocal and OCT enabled simultaneous *en face* [Fig. 3.2(D)] and cross-sectional [Fig. 3.2(E)] measurements. For each experiment, 100-ms pre-stimulus and 400-ms post-stimulus images were recorded at the speed of 200 frames per second. A 10-ms oblique stimulus [Fig. 3.2(A), 20° or −20°, $2×10^5$ photons/μm^2/ms] was introduced to stimulate the retina. Transient photoreceptor displacement could be observed after the delivery of the retinal stimulation [see Media 1, Fig. 3.2(E)]. In order to quantify the photoreceptor displacement, we adopted the optical flow code developed by Sun et al. [104]. Optical flow is a well-established method for calculating target movements between two images. It can accurately identify movements of fine details in sequential images, which makes the method suitable for tracking small movements of retinal cells. Stimulus-evoked transient photoreceptor displacements could be quantified in magnitude and direction maps. In order to automatically segment active area and inactive area in displacement magnitude map, we used the classic automatic thresholding method for bi-modal images: Otsu's method [105]. Segmented active area was color coded in the direction map according to predefined scale [Fig. 3.2(B)]. The inactive area in direction map was coded as black.

Figure 3.3(A) illustrates confocal and OCT results of the retina stimulated with 20° and −20° oblique light flashes. The results were calculated from the average of 10 images acquired between 100 ms and 150 ms after the onset of the stimulus light. As shown in Figs. 3.3(A3) and 3.3(A4), dynamic confocal imaging revealed that retinal photoreceptors moved toward the 0° direction, i.e., right direction, corresponding to the 20° oblique stimulation. In other words, the photoreceptor moved toward the incident light, which was consistent with our early observation using a digital NIR microscope [74]. Cross-sectional retinal OCT images revealed that the TRP primarily localized at the photoreceptor outer segment [Figs. 3.3(A6) and 3.3(A7)]. The OCT images in Figs. 3.3(A7) and 3.3(A8) confirmed that the 20° stimulation led the photoreceptor to shift right, i.e., toward the direction of stimulus light.
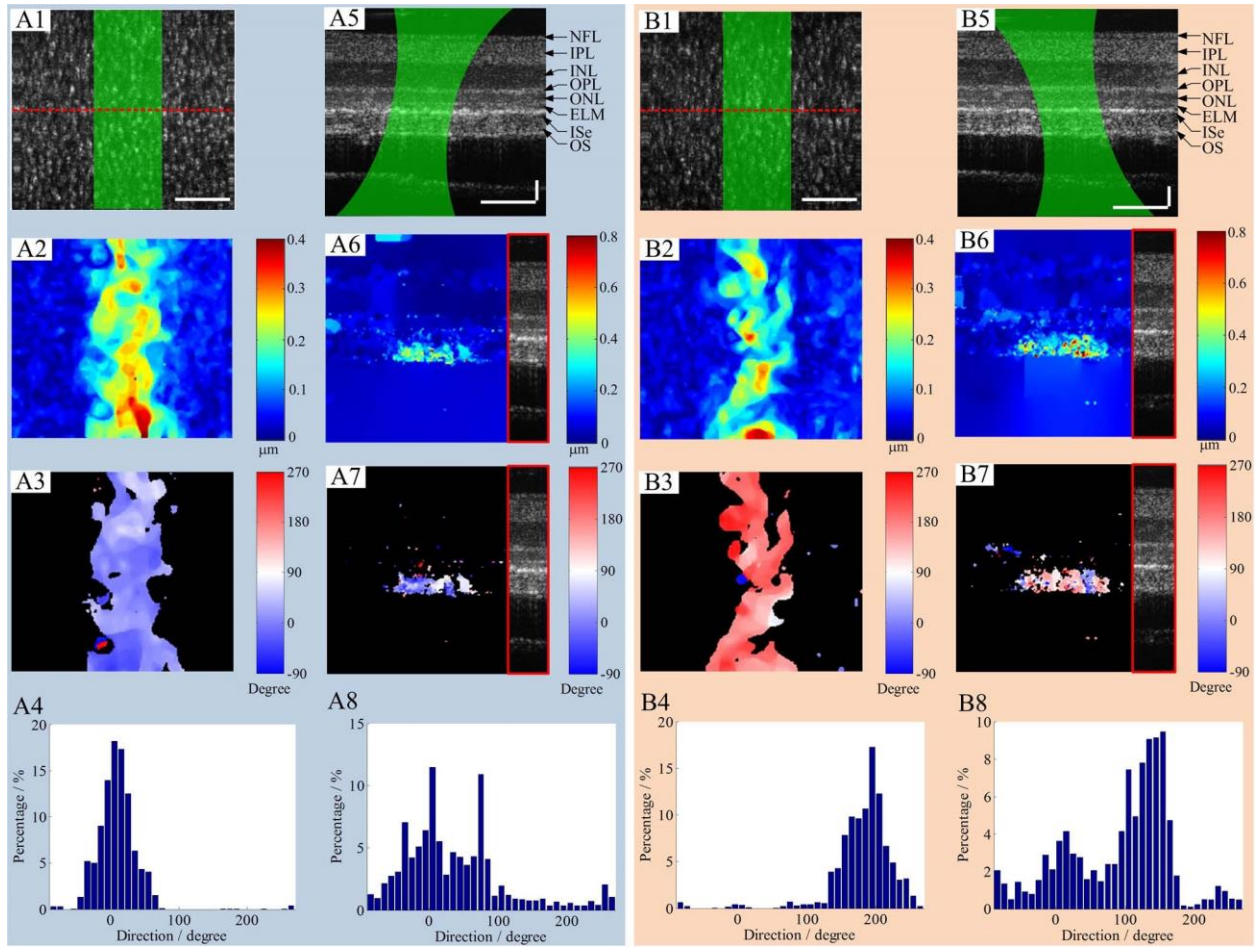
Fig. 3.3 Magnitude and angle of TRP evoked by 20° and -20° stimulation. (A) Confocal and OCT observation of the TRP evoked by 20° oblique stimulation. (A1) Confocal image of retinal photoreceptors. Green rectangle represents the 20° oblique stimulus light. Red dashed line shows the location for OCT recording (A5). (A2) TRP magnitude map derived from confocal images. (A3) TRP direction map derived from confocal images. Inactive area is mapped by black background. Active/inactive areas are separated according to displacement magnitude map (A2) by using Otsu's thresholding method. Active area is the location with detectable photoreceptor displacement, while inactive area is the location without detectable displacement. (A4) Histogram of TRP directions in (A3). (A5) Cross-sectional retinal OCT image. The green area indicates the 20° oblique stimulus. (A6) TRP magnitude map derived from OCT images. OCT cross-sectional image is merged in the red rectangle for easy identification of axial location of detectable displacement. (A7) TRP direction map derived from OCT images. (A8) Histogram of TRP directions in (A7). (B) Confocal and OCT observation of the TRP evoked by −20° oblique stimulation. (B1) Confocal image of photoreceptors. Green rectangle represents −20° oblique stimulus light. Red dashed line shows the location for OCT recording (B5). (B2) TRP magnitude map derived from confocal images. (B3) TRP direction map derived from confocal images. (B4) Histogram of TRP directions in (B3). (B5) Cross-sectional retinal OCT image. The green area indicates the −20° oblique stimulus. (B6) TRP magnitude map derived from OCT images. (B7) TRP direction map derived from OCT images. (B8) Histogram of TRP directions in (B7). Scale bars: 50 μm.

In order to further verify the orientation dependence of the TRP, we switched stimulus light direction from 20° to −20°. As shown in Figs. 3.3(B1)–3.3(B8), the TRP was consistently observed in the stimulated area (Fig. 3.3(B2)). Figure 3.3(B3) shows that displacement angle was ~180°, which indicated the photoreceptors moved left due to −20° stimulation. The cross-sectional retinal OCT images [Fig. 3.3(B7)] also consistently revealed the orientation dependence of the TRP. It was observed that when the stimulus light changed from 20° to −20°, photoreceptor displacement direction switched from right to left. In other words, when stimulus light direction was reversed, photoreceptor displacement direction was also reversed. Figure 3.3(B6) confirmed that the photoreceptor displacement started from IS/OS junction and primarily occurred at the OS.

3.4 Discussion

In summary, the TRP was consistently observed in both *en face* confocal and cross-sectional OCT images. Comparative analysis of the confocal and OCT images indicated that the TRP was orientation dependent, i.e., the photoreceptor moved toward the direction of oblique stimulus light. Although both confocal and OCT measurements revealed convincible TRP changes, some slight difference was observed. For confocal data, it was observed that the distribution of the TRP direction was approximately normally distributed with a mean value of 0° (right movement) or 180° (left movement) [Figs. 3.3(A4) and 3.3(B4)]. However, the distribution of the TRP direction in OCT data slightly deviated away from normal distribution [Figs. 3.3(A8) and 3.3(B8)]. Most likely, this is due to different signal-to-noise ratios (SNRs) of the confocal and OCT images. It is known that the OCT images were severely affected by speckle noise [106]. Moreover, the confocal image was recorded from a relatively large area, and average effect might enhance relative SNR. Depth-resolved OCT imaging unambiguously revealed that the TRP was predominantly occurred at photoreceptor OS. Although we do not totally understand the mechanism underlying this phenomenon, an early study has reported disc-

shape change of photoreceptor rod [92]. Orientation unbalanced disc-shape change might contribute to the observed TRP. We speculated that the TRP may compensate for some part of the light efficiency loss caused by oblique illumination. We are currently pursuing comparative TRP imaging and electrophysiological measurement for better investigation of anatomical source and biophysical mechanism of the TRP. This is not only important for better understanding of the SCE on rod and cone systems, but can also be essential for establishing an intrinsic biomarker for early detection of eye diseases that can produce photoreceptor dysfunctions. Many eye diseases, such as age-related macular degeneration (AMD), can produce photoreceptor damages associated with severe vision loss including legal blindness. Currently, there is no outright cure for the retinal degenerative. A key strategy for preventing vision loss due to late AMD is to preserve function and be vigilant for changes in early AMD signifying progression. It is well established that physiological integrity of rod photoreceptors is more vulnerable than that of cones in early AMD [4, 5]. Therefore, the rod-dominant TRP promises a new strategy to allow objective assessment of localized rod dysfunctions at high resolution.

Acknowledgment

CHAPTER IV. *IN VIVO* OPTICAL COHERENCE TOMOGRAPHY OF STIMULUS EVOKED INTRINSIC OPTICAL SIGNALS IN MOUSE RETINAS

(Previously published as B. Wang, Y. Lu, and X. Yao (2016) *In vivo* optical coherence tomography of stimulus evoked intrinsic optical signals in mouse retinas. *Journal of Biomedical Optics* 21(9), 096010 [3])

Abstract: Intrinsic optical signal (IOS) imaging promises a noninvasive method for advanced study and diagnosis of eye diseases. Before pursuing clinical applications, it is essential to understand anatomic and physiological sources of retinal IOSs and to establish the relationship between IOS distortions and eye diseases. The purpose of this study was designed to demonstrate the feasibility of *in vivo* IOS imaging of mouse models. A high spatiotemporal resolution spectral domain optical coherence tomography (SD-OCT) was employed for depth-resolved retinal imaging. A custom-designed animal holder equipped with ear bar and bite bar was used to minimize eye movements. Dynamic OCT imaging revealed rapid IOS from the photoreceptor's outer segment immediately after the stimulation delivery, and slow IOS changes were observed from inner retinal layers. Comparative photoreceptor IOS and electroretinography recordings suggested that the fast photoreceptor IOS may be attributed to the early stage of phototransduction before the hyperpolarization of retinal photoreceptor.

4.1 Introduction

Eye diseases, such as age-related macular degeneration (AMD) [4, 5], retinitis pigmentosa (RP) [6], diabetic retinopathy [7, 8], and glaucoma [9, 10] can produce retinal neural dysfunctions that lead to severe vision loss if appropriate interventions are not involved promptly. It is known that different eye diseases damage different retinal cells, which are located in different functional layers. For example, retinal photoreceptors are vulnerable in AMD [4] and ganglion cells are affected in glaucoma [10]. Electroretinography (ERG) [11] and multifocal ERG [18, 19] can

provide objective evaluation of retinal neural dysfunction, but the spatial resolution is limited due to the integral effect of bioelectric signals from multiple retinal layers. Each hexagonal stimulus pattern used in multifocal ERG usually has an angular size of ~5 deg [18, 19], corresponding to ~2 mm resolution in the human retina. Therefore, accurate separation of ERG components of retinal neurons is difficult. The low signal selectivity of ERG due to the integral effect makes its interpretation complicated for clinical diagnoses. Optical methods, such as fundus photography and optical coherence tomography (OCT) [17], can provide high-resolution examination of retinal morphology. However, morphological images do not directly provide functional information of retinal physiology. A high-resolution method for objective evaluation of retinal physiological function is desirable for early disease detection and improved treatment evaluation.

Intrinsic optical signal (IOS) imaging has promise as a high resolution method for objective assessment of retinal neural dysfunctions due to eye diseases [57]. Micrometer level (<3 µm) resolution has been achieved for *in vivo* IOS imaging of frog retinas using custom-designed confocal [12] and OCT [16] systems. Stimulus-evoked IOSs have been observed in multiple animal models [1, 12-16, 60-69, 107] and human subjects [70]. Recent OCT studies revealed rapid IOS changes at photoreceptor outer segments [1, 16]. *In vitro* IOS imaging of normal and mutant mouse retinas has been conducted to demonstrate disease-produced IOS distortions [73]. Laser injured frog eyes have been used to demonstrate *in vivo* IOS mapping of localized retinal dysfunction [14]. Both *in vitro* and *in vivo* studies have shown that fast IOSs have different polarities and mainly originate from the photoreceptor outer segments in frog retinas [57]. These studies also revealed that photoreceptor IOSs had a rapid time course (<4 ms after onset of the light stimulus) [1, 16]. Transient retinal phototropism was reported to be one factor that generates photoreceptor IOSs [2, 74, 108], but the IOS physiological source has not been accurately determined yet. Before pursuing clinical applications, it is necessary to establish the relationship between IOS distortions and eye diseases. Multiple mouse models are available to

characterize IOS abnormalities in diseased retinas. However, *in vivo* IOS imaging of mouse retinas is technically difficult due to small the ocular lens and inevitable eye movements.

The purpose of this study was designed to demonstrate the feasibility of *in vivo* IOS imaging of mouse models. Some part of the results has been reported in the SPIE Proceedings [109]. To achieve high spatiotemporal resolution imaging, a high-speed [up to 1250 frames per second (fps)] and high-resolution ($\sim$3 μm in both lateral and axial directions) spectral domain OCT (SD-OCT) was constructed. Comparative IOS and ERG measurements were conducted to investigate the physiological mechanism of retinal IOSs.

4.2 Methods

4.2.1 Experimental Setup
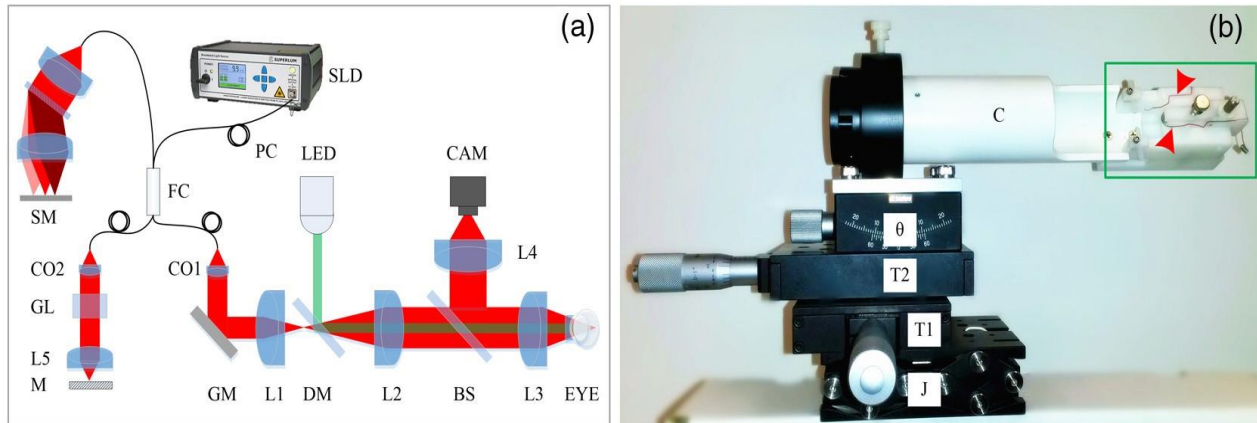
Fig. 4.1 *In vivo* SD-OCT setup. (a) Schematic diagram of the custom-designed OCT used for *in vivo* IOS imaging of mouse retinas. SLD: superluminescent diode; SM: spectrometer; PC: polarization controller; FC: 90:10 fiber coupler; CAM: camera; LED: light-emitting diode; CO1–CO2: collimators; L1–L5: lenses; GL: glass blocks; M: mirror; GM: galvo mirror; DM: dichroic mirror; BS: beam splitter. (b) Photograph of the custom-designed animal holder. J is a mini lab jack for z adjustment, T1 and T2 are translational stages for x and y adjustments, θ is the θ translation stage for pitch adjustment, C is the mouse cassette where the mouse was placed. The green rectangle shows the bite bar and ear bar unit. The red arrowheads indicate the ERG electrodes.

Figure 4.1(a) shows a schematic diagram of our custom-designed SD-OCT. A wide bandwidth near-infrared (NIR; $\Delta\lambda$=100 nm, λ=850 nm) superluminescent diode (SLD; D-840-HP-I, Superlum) was used as the OCT light source to provide high axial resolution (~3 µm). The NIR light was focused on the retina through optical lenses and the mouse eye and was scanned with a galvo mirror (GVS001, Thorlabs, Inc.) to produce OCT B-scan images. The pivot of the galvo mirror and the pupil of the mouse eye were placed conjugate to each other in order to minimize the vignetting effect. The lateral resolution of the system was about 3 µm. A green (λ= 505 nm) light emitting diode (LED; M505L3, Thorlabs, Inc.) was coupled to the imaging system with a dichroic mirror (DMLP650R, Thorlabs, Inc.) for retinal stimulation. For easy alignment of the mouse eye, a pupil camera was integrated into the system. A custom-designed spectrometer was constructed for OCT recording. The linear camera (EV71YEM4CL2014BA9, e2v) used in the OCT provided a line rate up to 70,000 lines/s. The high imaging speed minimized the in-frame image blur and between-frame displacement, thus reduced the effect of eye movements to enable robust observation of IOS responses correlated with retinal stimulation.

Figure 4.1(b) shows a photograph of our custom-designed animal holder. Since IOSs measure pixel intensity changes in captured images, the IOS imaging quality is extremely sensitive to movements. Eye movements caused by the breath and heartbeats can be significant if the mouse head is not appropriately fixated. The combined bite bar and ear bar system has been used in stereotaxic surgeries [110, 111]. However, commercial stereotaxic frames cannot be directly used for mouse imaging because they do not provide enough degrees of freedom to align the mouse eye for OCT recording. To achieve a robust IOS recording, we designed an animal holder with five degrees of freedom (i.e., *x*, *y*, *z*, pitch, and roll) and integrated the bite bar and ear bar system. Two linear translation stages and one mini lab jack were used to provide *x*, *y*, and *z* alignments, a *θ* translation stage was used for pitch alignment, and a

cassette was used to provide roll adjustment of the imaged mouse. The bite bar and ear bar system was fixed at the end of the cassette.

4.2.2 Animal Preparation

Adult (3 to 6 months old) wild-type mice (strain C57BL/6J, The Jackson Laboratory) were used in this study. Before the experiment, each mouse was first dark or light adapted (~500 cd/m^2) for 3 h, and then was anesthetized with 60 mg/kg ketamine and 3 mg/kg xylazine given by intraperitoneal injection. After the mouse was fully anesthetized, it was transferred to the custom designed animal holder with the head fixed by an ear bar and bite bar. A drop of 1% atropine was applied to the mouse eye for pupil dilation. An ERG active electrode was placed in contact with the cornea. One drop of ophthalmic gel was applied to each eye to keep them from clouding. A cover glass was placed on the imaged eye ball. The cover glass along with the gel worked as a contact lens to improve image resolution by reducing optical aberrations of the mouse eye [112]. During the recording, a heating pad was wrapped around the animal holder to keep the mouse warm. All experiments were performed following the protocols approved by the Animal Care Committee at the University of Illinois at Chicago.

4.2.3 Data Acquisition

For IOS measurement, OCT images in Fig. 4.3 were recorded at 200 fps. After a 1-s pre-stimulus recording, a 10-ms light flash, with different intensities varying 20 dB (−20, −16, −13, −9.5, −6.3, −2.6, and 0 dB relative to maximum intensity, where the maximum intensity of 0 dB was measured 2 × 10^7 photons · μm^{-2}· ms^{-1} on cover glass) was introduced for retinal stimulation. After the onset of the stimulus, OCT images were recorded for 4 s. For high-speed IOS recording (Fig. 4.6), the line number in OCT B-scans was reduced so that recording speed increased to 1,250 fps. A −9.5 dB 10-ms flash was introduced after an 80-ms pre-stimulus recording. IOSs were recorded for 160 ms after onset of the stimulus. All data were saved to a

computer hard drive for post processing. Although a head fixation method was used, there was still detectable bulk motion in the OCT images. Residual bulk motion was digitally compensated for by accurate image registration using an algorithm described in a previous publication [16]. Subsequently, the OCT images were then used for calculating IOSs using a custom developed MATLAB® (MathWorks, Natick, Massachusetts) program. The data processing procedure has been described previously [103].

For ERG recording, a silver electrode with the tip bent to a ring was placed in contact with the mouse cornea and served as an active electrode; a silver reference electrode was twisted on the bite bar so that it contacted the mouse mouth reliably when the head was fixed. ERG recordings were amplified 1,000 times and filtered (pass band: 1 to 1,000 Hz) by a differential amplifier (DAM50, World Precision Instruments). The amplified and filtered ERG recordings were then sampled by a data acquisition board (PCIe-6351, National Instruments) at 40,000 samples/s and saved to a computer hard drive.

4.3 Results
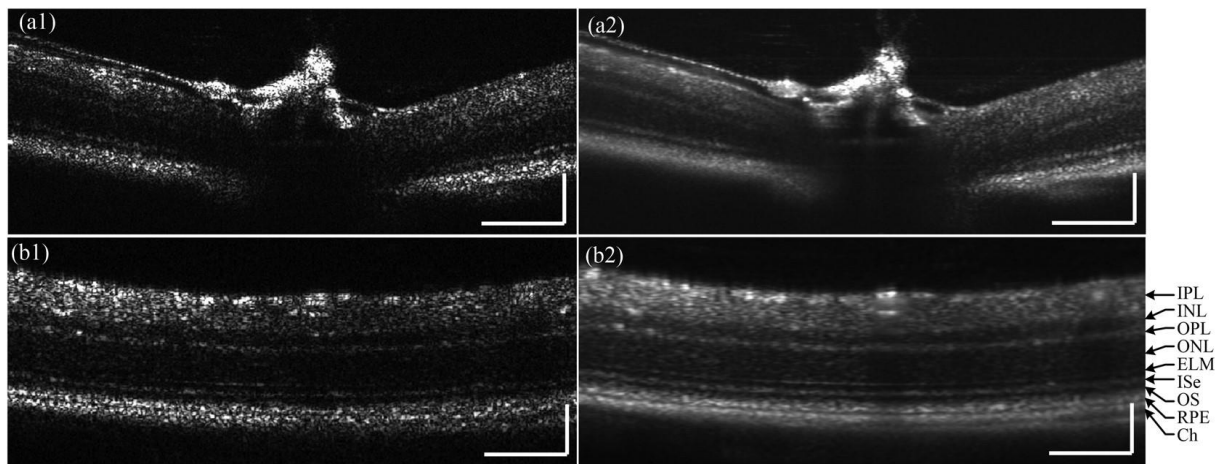
Fig. 4.2 Mouse retinal B-scans acquired with the custom-built SD-OCT. (a1) Single frame retinal B-scan of the optic nerve head, and (a2) average of 10 frames. (b1) Single frame retinal B-scan ~0.6 mm away from the optic nerve head, and (b2) average of 10 frames showing clear retinal layers including the: IPL: inner plexiform layer, INL: inner nuclear layer, OPL: outer plexiform layer, ONL: outer nuclear layer, ELM: external limiting membrane, ISe: inner segment ellipsoid, OS: outer segment, RPE: retinal pigment epithelium, and Ch: choroid. Scale bars: 100µm.
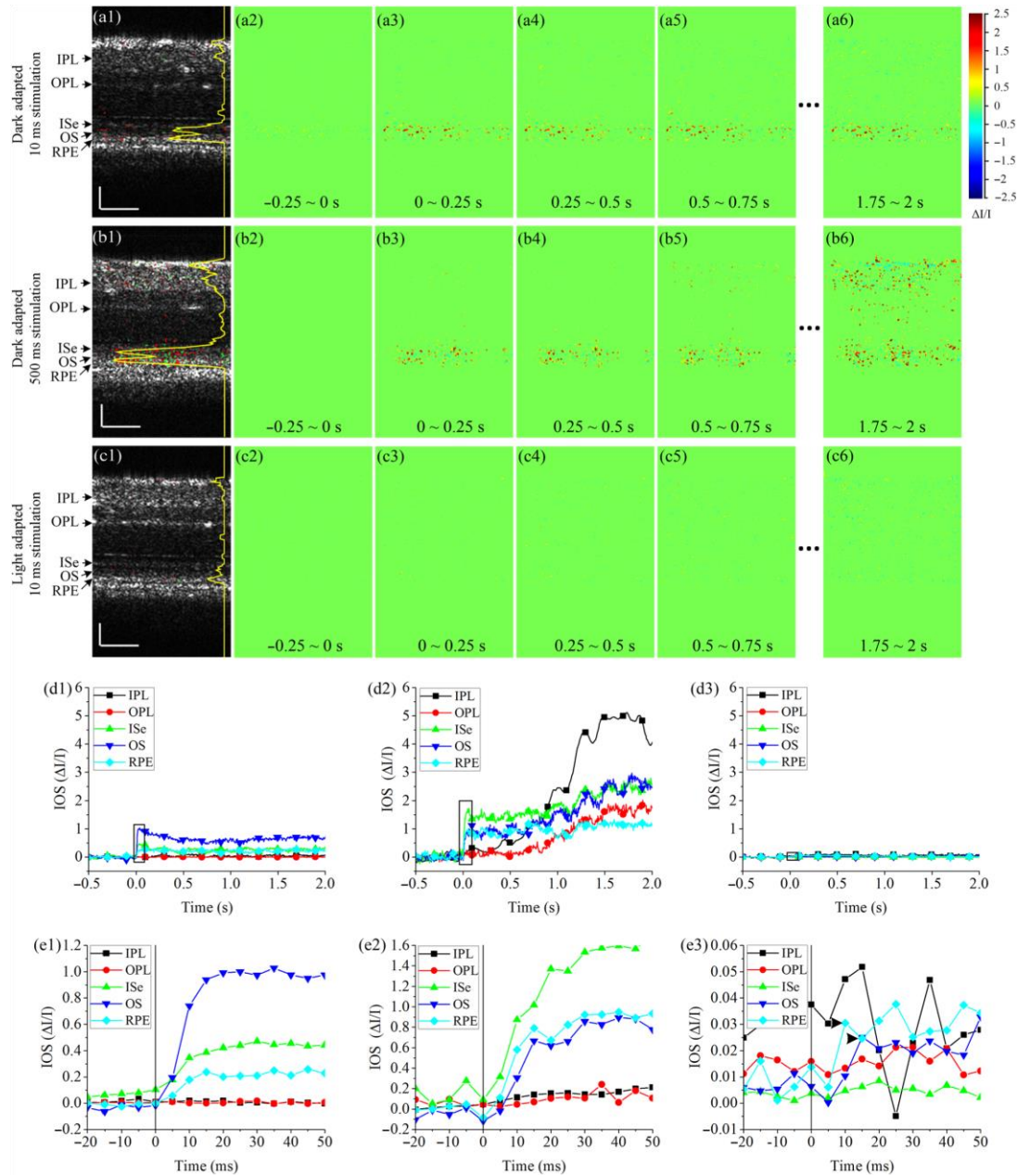
Fig. 4.3 Representative *in vivo* IOS imaging results under different stimulation and light adaptation conditions. Stimulation intensity was −9.5 dB. (a) IOS imaging results from dark adapted retina with 10-ms light stimulation. (a1) Activated pixels at 0.5 s. The yellow curve shows the active pixel number. (a2)–(a6) IOS images at different times. (b) IOS imaging results from dark adapted retina with 500-ms light stimulation. (b1) Activated pixels at 0.5 s. The yellow curve shows the active pixel number. (b2)–(b6) IOS images at different times. (c) IOS imaging results from light-adapted retina with 10-ms light stimulation. (c1) activated pixels at 0.5 s. The yellow curve shows the active pixel number. (c2)–(c6) IOS images at different times. (d) Absolute IOS curves from different retinal layers calculated from experimental trials corresponding to panels (a), (b), and (c). IOS curves were normalized by multiplying the active pixel ratio in corresponding retinal layers. (e) Enlarged views of black rectangle areas in (d). (e1)–(e3) correspond to (d1)–(d3), respectively. Vertical lines show stimulus onset. Arrowheads in (e3) indicate IOS peaks. Scale bars in (a), (b), and (c): 50 μm.

Figure 4.2 shows a single frame and the average of 10 OCT B-scan images with a frame resolution of 600 pixels × 230 pixels. Figure 4.2(a) shows a representative B-scan around the optic nerve head. Figure 4.2(b) shows a B-scan ~0.6 mm away from the optic nerve head where individual retinal layers, including the inner plexiform layer (IPL), inner nuclear layer (INL), outer plexiform layer (OPL), outer nuclear layer (ONL), external limiting membrane (ELM), inner segment ellipsoid (ISe), outer segment (OS), retinal pigment epithelium (RPE) and choroid, were clearly observed. Averaged B-scans in Figs. 4.2(a2) and 4.2(b2) show a clearer layered structure due to an increased signal to noise ratio (SNR).

Figure 4.3 shows representative IOS results from different stimulation and light adaptation conditions. In dark adapted retinas, robust rapid IOSs were observed from photoreceptor outer segments immediately after stimulation delivery [Figs. 4.3(a) and 4.3(b)]. Unambiguous IOS changes, with a delayed time course, were also observed from the IPL in the retina with 500-ms stimulation [Figs. 4.3(b5) and 4.3(b6)]; while no reliable IOSs from the IPL were observed in the retina with 10-ms stimulation. The yellow curve in Fig. 4.3(b1) shows more activated pixels at 0.5 s in outer retinal layers under 500-ms stimulation than those in Fig. 4.3(a1) under 10-ms stimulation. When the retina was light adapted and rods were bleached, no IOS response was observable from the IOS images [Figs. 4.3(c2)–4.3(c6)]. We plotted IOS curves from different layers, as shown in Fig. 4.3(d). The curves were calculated by averaging pixel intensities of all active pixels in corresponding layers [shown as green and red pixels in Figs. 4.3(a1), 4.3(b1), and 4.3(c1)]. The curves were then normalized by multiplying the active pixel ratio in corresponding retinal layers. Robust rapid IOSs were observed from ISe, OS, and RPE layers in dark adapted retinas [Figs. 4.3(d1) and 4.3(d2)] immediately after stimulus onset [Figs. 4.3(e1) and 4.3(e2)]. When the retina was stimulated with 500-ms light, robust slow IOSs were observed from the IPL [Fig. 4.3(d2)]. The IOS onset time from the IPL was ~0.5 s. In the light-adapted retina, IOSs of all retinal layers were hardly observable and magnitudes were relatively

small, compared to those in dark adapted retinas. Figure 4.3(e3) revealed low magnitude, rapid

IOS changes (arrowheads) immediately after stimulation delivery from the OS and RPE layers.

In vivo mouse IOS properties were similar to those we observed in frogs [16]. IOSs from outer

retinal layers shown in Fig. 4.3(e3) suffered from high noise level. To confirm the IOSs in light

condition, an additional seven experiments were conducted with light-adapted retinas. Figure

4.4 illustrates average IOS changes of eight retinas, and convincible IOS was observed from the

outer retina (i.e., ISe, OS, and RPE) immediately after the stimulation delivery.
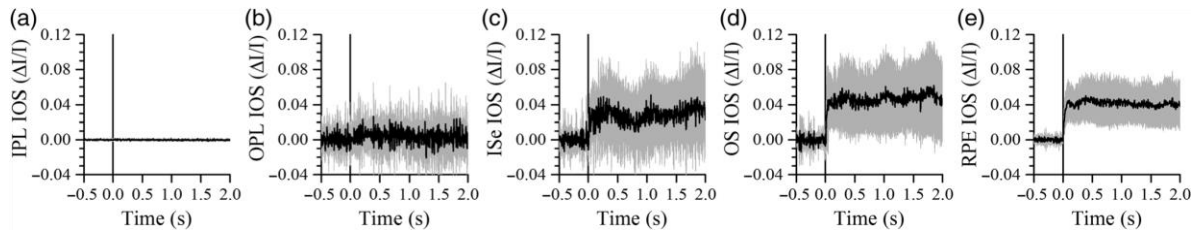
Fig. 4.4 Averaged IOSs of (a) IPL, (b) OPL, (c) ISe, (d) OS, and (e) RPE layers in light-adapted retinas. Each curve is average of eight experimental trials. Gray areas show standard deviation. Vertical lines show stimulus onset.
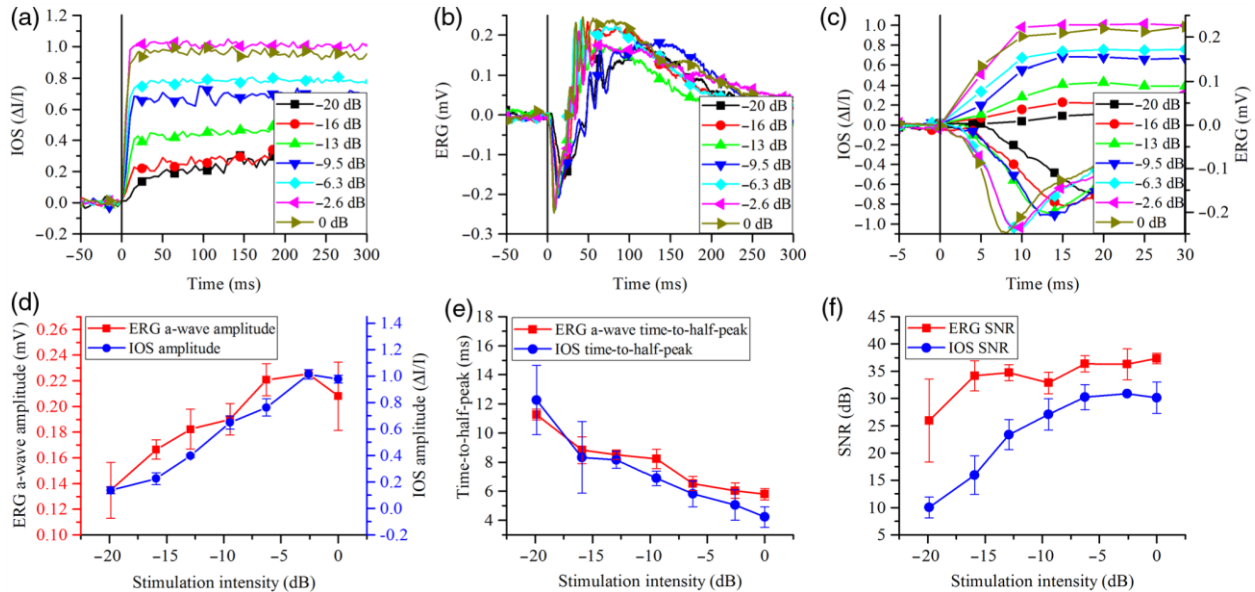
Fig. 4.5 Photoreceptor IOS and ERG responses under different stimulation intensities. (a) Absolute photoreceptor IOS curves under different stimulation intensities. Vertical line shows stimulus onset. Each curve represents an average of three experimental trials. (b) Representative ERGs under different stimulation intensities. The vertical line shows stimulus

onset. (c) Photoreceptor IOSs (curves above y=0) and ERGs (curves below y=0) from −5 to 30 ms. The vertical line shows stimulus onset. (d) ERG a-wave and photoreceptor IOS amplitude changes as a function of stimulation intensity. (e) ERG a-wave and photoreceptor IOS time-to-half-peak changes as a function of stimulation intensity. (f) Photoreceptor IOS and ERG SNR changes as a function of stimulation intensity.

Photoreceptor IOS and ERG a-wave responses to different stimulation conditions were recorded to investigate the IOS physiological origin in mice. The retinas were stimulated by 10-ms light flashes with intensities varying 20 dB. Three trials were conducted for each stimulation intensity. Figure 4.5(a) shows averaged photoreceptor IOS curves and Fig. 4.5(b) shows representative single trial ERG curves at different stimulation intensities. It was observed that the amplitude and time scales of photoreceptor IOS and ERG a-wave were both dependent on the stimulation intensity. The dependency was shown more clearly in the enlarged view in Fig. 4.5(c). Figure 4.5(c) also showed that photoreceptor IOSs appeared earlier than ERG a-waves under the same stimulation intensity. From Fig. 4.5(d), we can see that photoreceptor IOS and ERG a-wave amplitudes changed very similarly; i.e., both increased as stimulation intensity increased and reached a peak at −2.6 dB stimulus intensity. As photoreceptor IOS amplitudes increased, the IOS SNR also increased and reached a peak at −6.3 dB stimulation intensity [Fig. 4.5(f)]. Photoreceptor IOS and ERG a-wave time-to-half peak (time for IOS or ERG a-wave to reach half maximum) responded similarly to stimulation intensity, i.e., both decreased as stimulation intensity increased [Fig. 4.5(e)].

To further understand the physiological source of photoreceptor IOS, we increased IOS imaging speed to detect the photoreceptor IOS and ERG a-wave onset times in dark adapted retinas. The onset time was defined as the time for photoreceptor IOS or ERG a-wave to reach the amplitude of 3σ, where σ was the standard deviation of the pre-stimulus IOS/ERG amplitude. Linear interpolation was used if 3σ fell between the observed data points. We chose a moderate stimulation intensity of −9.5 dB, which corresponded to the fourth data point in Figs. 4.5(d)–4.5(f). To increase IOS imaging speed, we decreased the A-line number and increased the IOS
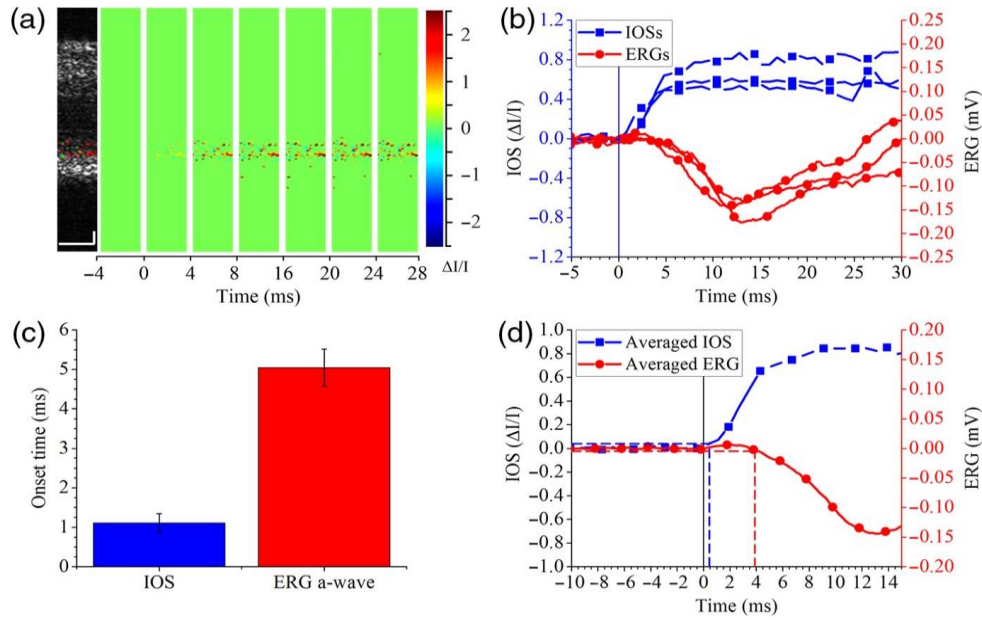
Fig. 4.6 Comparison of time courses between IOS acquired at 1,250 fps and ERG. (a) IOS imaging with 1,250 fps OCT. (b) Photoreceptor IOS and ERG changes. IOSs and ERGs were recorded from three different retinas. Vertical line shows stimulus onset. (c) Comparison between average photoreceptor IOS and ERG a-wave onset times. (d) Averaged photoreceptor IOS and ERG corresponding to the IOS and ERG curves in (b). Vertical solid line shows stimulus onset. Horizontal dashed lines show 3σ of pre-stimulus IOS (blue) and ERG (red) amplitudes. Vertical dashed lines show IOS (blue) and ERG (red) onset times. Scale bars in (a): 25 μm.

imaging speed from 200 to 1,250 fps; the corresponding time resolution was increased from 5 to 0.8 ms. Figure 4.6(a) shows the IOS map and IOS images acquired at 1,250 fps. Three photoreceptor IOS and ERG curves recorded from different retinas were plotted together for comparison in Fig. 4.6(b). It was clearly observed that photoreceptor IOS onset time was shorter than ERG a-wave onset time. Onset time of each curve in Fig. 4.6(b) was calculated and then averaged for quantitative comparison in Fig. 4.6(c). We can see that the photoreceptor IOS onset time was 1.1±0.2 ms, while the ERG a-wave onset time was 5.0±0.5 ms [113]. The difference was statistically significant with a p-value smaller than 0.001 using a single sided t-test. Figure 4.6(d) shows the averaged photoreceptor IOS and ERG curves. The vertical dashed lines show onset times calculated based on the averaged curves. As a result of averaging, noise level was reduced, thus the 3σ was reduced, resulting in smaller calculated onset times. It

is shown that the photoreceptor IOS onset time was as short as ~0.4 ms while ERG onset time was ~3.9 ms.

4.4 Discussion

In summary, the feasibility of *in vivo* IOS imaging of mouse models was demonstrated using a custom-designed functional OCT. We were aware of that head restraining devices; i.e., bite bar and ear bar, were essential for reducing eye movement to improve IOS quality. Photoreceptor IOS and ERG a-wave magnitude showed a similar response to variable stimulation intensity (Figs. 4.5(d)–4.5(e)]. High-speed (1,250 fps) IOS imaging revealed that the photoreceptor IOS onset time was ~1.1 ms, while the ERG a-wave onset time was ~5.0 ms at stimulation intensity of −9.5 dB.

Figures 4.3(d1) and 4.3(d2) show similar IOSs from RPE, OS and ISe layers in dark adapted retinas. We speculated that the RPE IOS were contributed by photoreceptor OSs because the OSs can penetrate into the RPE layer [114]. ISe IOS may also come from OSs because the ISe and OSs are immediately adjacent and the active pixels were mainly at the outer part of the ISe [yellow curves in Figs. 4.3(a1) and 4.3(b1)], which could actually be the OS because OCT axial resolution (~3 μm) was not high enough to differentiate those layers [91]. Thus, fast IOS observed was mainly from photoreceptor OS [16]. It is well established that ERG a-wave is the result of the phototransduction process in photoreceptor OS. It reflects the closure of cyclic guanosine monophosphate gated channels on photoreceptor membrane and dark current reduction due to light absorption in OS [41, 42]. Considering that both photoreceptor IOS and ERG a-wave are from OS and that photoreceptor IOS and ERG a-wave were closely correlated [Figs. 4.5(d)–4.5(e)], we speculate that the rapid photoreceptor IOS also originated from phototransduction processes.

From Fig. 4.5(c) we could see that photoreceptor IOS onset times were shorter than ERG a-wave onset times. High-speed OCT showed that photoreceptor IOS onset time was ~3.9 ms shorter [Fig. 4.6(b) and 4.6(c)] under −9.5 dB stimulation intensity. Since photoreceptor IOS onset time was shorter than ERG a-wave onset time, it suggests that the photoreceptor originated from the early stage of phototransduction before the hyperpolarization of the retinal photoreceptor, which generates ERG a-wave. According to Yoshizawa and Kandori [115], the time required for rhodopsin to absorb photons and become enzymatically active is around 1 ms. Figure 4.6(d) shows that, when averaged, photoreceptor IOS could be observed at ~0.4 ms, and this confirmed that photoreceptor IOS originated from early phototransduction.

Rapid IOSs were observed in light-adapted retinas from outer retinal layers [Figs. 4.3(d3) and 4.4(c)–4.4(e)]. Such signals possibly originated from cones in light-adapted retinas. Given the fact that cones only account for ~3% of all photoreceptors in mice, the total IOS in light-adapted retinas should be small, compared to that in dark adapted retinas. In animal models with more cones, e.g., frogs where cone ratio is ~50%, larger light-adapted IOS was observed [16]. The resolution of our current system is not high enough to directly differentiate mouse rods and cones (rod OS diameter ~1.4 μm, cone OS diameter ~1.2 μm [116]). Further investigation with adaptive optics OCT may enable further verification of the anatomic origination of the IOS changes.

In the retinas with prolonged stimulation, slow IOS was observed from inner retinal layers [Figs. 4.3(b) and 4.3(d2)]. We speculate that the slow IOS may involve the complications of nonlinear information processing in the retina as well as retina adaptation to stimulation. Light-induced hemodynamic change may also partially contribute to the slow IOS [59]. Further investigation is required to understand the origination of slow IOS.

Further *in vivo* and *in vitro* studies that use transgenic mouse models or use pharmacological agents to block specific phototransduction processes could help accurately identify photoreceptor IOS origination, and thus provide a method for advanced study and diagnosis of retinal diseases that cause photoreceptor dysfunction, such as AMD and RP. There are no readily available medicines or surgical procedures that could reverse photoreceptor degeneration and totally restore its function. The key to prevent vision loss is to diagnose retinal diseases in the early stages and apply intervention properly. By providing unparalleled spatial resolution and signal selectivity, we anticipate that further development of functional OCT of retinal IOSs will pave the way for early detection of retinal diseases and objective evaluation of clinical treatments.

4.5 Conclusion

This study demonstrates the feasibility of *in vivo* IOS imaging of mouse models using a custom-designed functional OCT. Comparative IOS imaging and ERG measurements suggest that the fast photoreceptor IOS may be attributed to the early stage of phototransduction before the hyperpolarization of the retinal photoreceptor. Further development of the functional OCT for *in vivo* IOS imaging of retinal photoreceptors may lead to a feasible method for objective assessment of retinal photoreceptor dysfunctions due to eye diseases.

Acknowledgment

CHAPTER V. FUNCTIONAL IMAGING OF THE RETINAL DEGENERATION 10 MOUSE RETINA USING FAST INTRINSIC OPTICAL SIGNAL

Abstract: The purpose of this study was to test the potential for using fast intrinsic optical signal (IOS) imaging for noninvasive detection and progression monitoring of retinal diseases. A custom-built high-speed (500 fps) and high-resolution (~3 µm) spectral domain optical coherence tomography (SD-OCT) device was used for *in vivo* mapping of fast IOS distortions in retinal degeneration 10 (rd10) mouse retinas from postnatal day 15 (P15) to P21. Simultaneous electrophysiological measurements were conducted by recording full-field electroretinograms (ERGs). Quantitative analysis revealed detectable functional fast IOS distortions, and OCT morphological abnormalities at P16 and P17, respectively. As retinal degeneration progressed, decreased fast IOS amplitudes were observed with a delayed time-course. Comparative electrophysiological measurements disclosed consistent abnormalities in the ERG a-wave, which is known to reflect retinal photoreceptor function. In conclusion, comparative morphological OCT and functional fast IOS imaging of WT and rd10 mice was conducted. The potential for using fast IOSs for early detection and progression monitoring of retinal photoreceptor degeneration was demonstrated.

5.1 Introduction

Retinal diseases; e.g. age-related macular degeneration (AMD) [4, 5] and retinitis pigmentosa (RP) [6], can damage the photoreceptors and ultimately lead to severe vision loss or even legal blindness if proper treatment is not applied in a timely manner. Since most of these vision impairments are not reversible, it is vital to detect retinal diseases at an early stage to allow prompt medical intervention. Both morphological assessment and functional examination are

important in retinal disease diagnosis. Fundus images [117, 118], scanning laser ophthalmoscopy (SLO) [119], optical coherence tomography (OCT) [17], and other assessments can provide high resolution evaluation of retinal morphology. Electroretinograms (ERGs) [11], multifocal ERGs [19], visual field tests [120], and other methods allow functional examination of visual physiology. However, separate morphological and functional tests increase the equipment complexity, testing times and costs. Moreover, it is complicated to establish a correlation between outcomes from different instruments. A new medical device that enables simultaneous morphological and functional imaging is desirable for the early detection of retinal diseases and reliable assessment of treatment outcomes.

Stimulus evoked intrinsic optical signals (IOSs), which reflect light property changes correlated with retinal physiological dynamics, have been obtained for evaluations. Because IOS images are reconstructed by dynamic computation of morphological images recorded during pre- and post-stimulus periods, IOS imaging naturally allows concurrent morphological and functional assessments. Functional IOS imaging has been demonstrated in different animal models including frogs [1, 3, 12-16, 57, 60-63, 103, 107], chickens [64, 65], rats [66], rabbits [67, 121], cats [68], primates [68, 69], and humans [70]. Both fast and slow IOSs have been observed. Early studies have revealed that slow IOSs mainly originate from the inner retina, while fast IOSs mainly originate from photoreceptor outer segments (OSs) [16, 121]. Since photoreceptor cells are vulnerable to many retinal diseases; e.g., AMD and RP, it is of high interest to study fast IOSs correlated with photoreceptor function. Stimulus-evoked photoreceptor OS changes, which could be a major source of fast IOSs in retinal photoreceptors, have been observed using different imaging modalities [2, 74, 108]. The physiological source of fast photoreceptor OS dynamics has been located to early phototransduction processes before hyperpolarization of photoreceptor cells [3, 122]. *In vivo* functional IOS imaging of laser-injured frog retinas has demonstrated IOS distortion correlated with localized laser damage [14]. *In vitro* imaging of

isolated retinas of *Cngb1* knock out mutant mice revealed distorted IOS and spontaneous response under wide-field microscope [73]. We have recently developed functional OCT to perform *in vivo* imaging of IOS responses in WT mouse retinas [109]. Here we describe functional OCT of IOS distortions in retinal degeneration 10 (rd10) mouse retinas, comparative electrophysiological measurements and retinal morphological evaluations.

5.2 Methods

5.2.1 Animal model

All animal experiments adhered to the ARVO Statement for the Use of Animals in Ophthalmic and Vision Research and were performed following the protocols approved by the Animal Care Committee at the University of Illinois at Chicago. Rd10 mice (strain: B6.CXB1-*Pde6b^{rd10}*/J, The Jackson Laboratory) were selected for studying retinal degeneration, and WT mice (strain: C57BL/6J, The Jackson Laboratory) were selected as a control group. The rd10 mouse is a disease model for human autosomal recessive RP [26]. Retinal degeneration in rd10 mice results from a spontaneous missense point mutation in the *Pde6b* gene [β-subunit of the rod cyclic guanosine monophosphate (cGMP) phosphodiesterase (PDE) gene] [123, 124]. PDE activity is reduced because of the mutation. PDE catalyzes the degradation of cGMP to guanosine-5'-monophosphate (5'-GMP) in the phototransduction process. Reduced activity of PDE causes the accumulation of cGMP, and ultimately photoreceptor death. The onset of retinal degeneration in rd10 mice is relatively slow compared to retinal degeneration 1 (rd1) mice, which allows a time window to monitor the progression of retinal degeneration using *in vivo* imaging instruments. At postnatal day 14 (P14) when the eye opens, the retinal structure of rd10 mice is comparable to that of WT mice. By P18, rd10 mice show loss of the inner segment/outer segment (IS/OS) junction and a significant decrease in thickness. The ERG of rd10 mice is never normal [125, 126].

5.2.2 Experimental setup

This study used the same experimental system that was used in Chapter IV. The system setup was described in detail in Chapter IV Methods section [109]. The *in vivo* SD-OCT provides a 3 μm resolution in both lateral and axial directions, with an imaging speed up to 70,000 A-lines per second. The ERG recording system was integrated for concurrent electrophysiological measurements. The active ERG electrode was made with a gold wire that was bent into a circle and placed in tight contact with the cornea of the mouse eye. The reference electrode, also gold wire, was twisted around the bite bar and was in contact with the mouth when the mouse was mounted to an animal holder. The ERG was amplified and filtered using an amplifier (DAM50, World Precision Instruments). The amplification was set to 1000×, and filter pass band was set to 1 Hz - 1 kHz. Amplified and filtered ERG was then digitized and sampled (sampling rate: 70k samples/s) by a data acquisition board (PCIe-6351, National Instruments). Both SD-OCT and ERG data were saved to a hard drive for post-processing.

5.2.3 Animal preparation

The mouse pups were reared under a 7/17 hour light-dark cycle (dark adaptation and data acquisition time counted in dark time). Before data acquisition, the mice were placed in the dark for 3 hours to ensure adequate dark adaptation. The experiment was conducted in a dark room illuminated with dim red light. The mouse was first anesthetized with 60 mg/kg ketamine and 3 mg/kg xylazine given by intraperitoneal injection. Then a drop of 1% atropine sulfate ophthalmic solution was applied to the imaging eye to dilate the pupil. After the pupil was fully dilated, the mouse was mounted onto the animal holder. An active ERG electrode was placed in contact with the cornea. A drop of eye gel was applied on both eyes and a cover glass was placed on the imaging eye.

5.2.4 Data acquisition

Retinal imaging and ERG measurements were acquired daily from P15 to P21. To minimize the effect of anesthesia to retinal development, a litter of pups were randomly separated to two groups. Data

were acquired from group 1 at P15, P17, and P19, and from group 2 at P16, P18, and P21. One thousand OCT images were continuously acquired at 500 frames per second. The ERG was recorded simultaneously. At 400 ms after the OCT recording started, a 10 ms green flash generated by a 505 nm LED (M505L3, Thorlabs) was introduced to stimulate the retina. The photon density delivered to the retina for stimulation was ~2.5×10^8 photons/μm^2. The weighted light radiance on the retina was ~10^{-5} J/mm^2, which was ~190 times lower than the safety standard [127].

5.2.5 IOS data processing

IOS images and curves were constructed from OCT images. Details of IOS data processing have been described in previous publications [16, 73]. Briefly, the steps to calculate IOS images from acquired OCT images were:

1) Obtain the baseline image $I_0(x,y)$ by averaging pre-stimulus OCT images $I_t(x,y)$.

2) Calculate the IOS image at time t using the equation:

$$IOS_t\left(x, y\right) = \frac{I_t\left(x, y\right) - I_0\left(x, y\right)}{I_0\left(x, y\right)}$$

(5.1)

To calculate IOS curves from acquired OCT images:

1) Obtain the baseline image $I_0(x,y)$ by averaging pre-stimulus OCT images $I_t(x,y)$; Calculate the standard deviation of each pixel $\sigma(x,y)$ from the pre-stimulus images.

2) Select positive and negative pixels using the 3-σ standard. For each pixel in each OCT image, if $I_t(x,y) > I_0(x,y) + 3\sigma(x,y)$, the pixel is a positive pixel. If $I_t(x,y) < I_0(x,y) - 3\sigma(x,y)$, the pixel is a negative pixel. Other pixels are inactive pixels. To reduce the possibility that an inactive pixel is identified as a positive or negative pixel, a pixel is identified as positive or negative only if it meets the 3-σ standard in 5 consecutive images.

3) Calculate the average intensity curves of the positive and negative pixels. Positive/negative pixels in each image are averaged and the average intensity curves of positive [$I_P(t)$] and negative pixels [$I_N(t)$] over time are acquired.

4) Calculate the baseline intensity I_0 of $I_P(t)$ and $I_N(t)$ by averaging the pre-stimulus data points.

5) Calculate the IOS curves using the following equation:

$$IOS(t) = \frac{I(t) - I_0}{I_0}$$

(5.2)

where $I(t)$ is $I_P(t)$ or $I_N(t)$.

5.2.6 Statistical analysis

Statistical analysis was implemented by conducting a one-tailed Welch's t-test [128], which assumes unequal variances. Analyzed parameters of WT and rd10 mouse retinas include: retinal thickness, ERG a-wave amplitude, ERG a-wave time-to-peak, IOS amplitude, and IOS time-to-half-peak. The parameters were considered significantly different between WT and rd10 mice if the p-value given by Welch's t-test was smaller than 0.05.

5.3 Results

5.3.1 OCT imaging of retina morphology

Using the custom designed SD-OCT, *in vivo* retinal OCT images of both WT and rd10 mouse were acquired at an imaging speed of 500 frames per second. Figure 5.1 shows representative retinal OCT images collected from WT and rd10 mice at ages from P15 to P21. Retinal OCT images clearly showed a layered structure and layer thickness changes of the retina over time. Retinal images of WT mice are shown in Figure 5.1(A). No obvious thickness change could be observed over time. Figure 5.1(B) shows the retinal images of rd10 mice. Significant thickness decreases were observed beginning from P17. Figure 5.1(C) illustrates thickness (manually measured from NFL to RPE) comparisons between WT and rd10 mice. The thickness of rd10 mouse retinas was close to that of WT mouse retinas at P15 and P16 ($p>0.05$). Between P16 and P17, the thickness of rd10 mouse retinas decreased ~60 μm and became significantly thinner than WT mouse retinas ($p<0.01$). Figure 5.1(D) shows thickness changes of different retinal layers in rd10 mouse retinas. Inner segment

ellipsoid (ISe) and photoreceptor outer segment (OS) layers were measured together because it was difficult to differentiate them in rd10 mouse retinas after P17. Most significant thickness decreases were observed in the OS and outer nuclear layer (ONL). Abrupt thickness changes of the OS were observed between P16 and P17, and abrupt thickness changes of the ONL were observed between P16 and P18. The results agreed with previous studies [126].
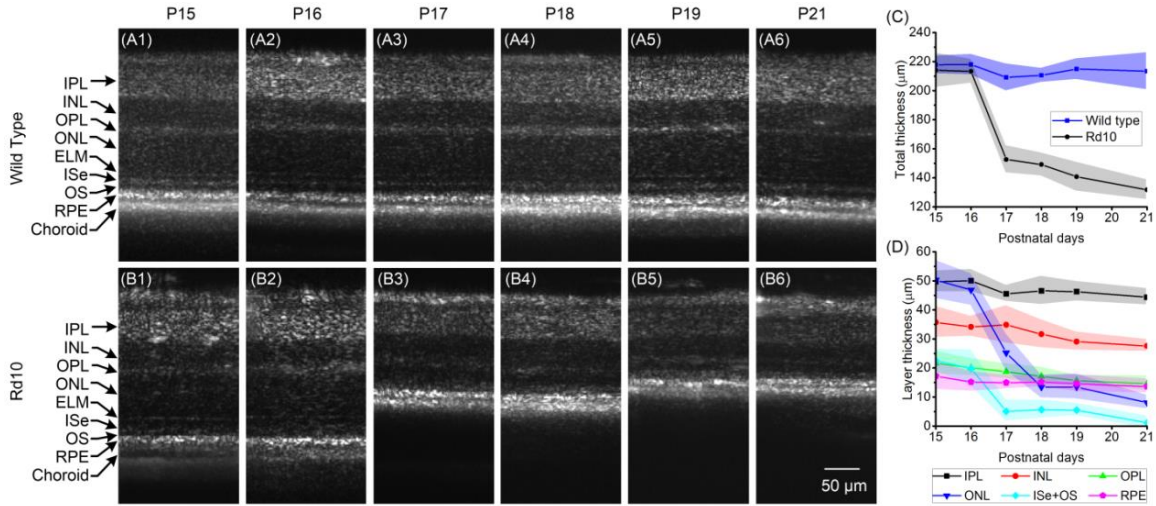

Fig. 5.1. Retinal thickness changes of WT and rd10 mice. (A) Representative OCT images of WT mouse retinas from different mice at different ages. IPL: inner plexiform layer; INL: inner nuclear layer; OPL: outer plexiform layer; ONL: outer nuclear layer; ELM: external limiting membrane; ISe: inner segment ellipsoid; OS: photoreceptor outer segment; RPE: retinal pigment epithelium. (B) Representative OCT images of rd10 mouse retinas from different mice at different ages. (C) Average total retina thickness changes of WT and rd10 mice from P15 to P21. Shades show the standard deviation. The number of WT mice was 8, and the number of rd10 mice was 10. (D) Average thickness changes of different retinal layers of rd10 mice from P15 to P21. Shades show the standard deviation. The thicknesses were measured manually.

5.3.2 Functional IOS imaging and comparative ERG

Figure 5.2 (A) and (B) show representative IOS images of WT and rd10 mice at different ages. The absolute IOSs were used; i.e., negative IOSs were multiplied by -1 while positive IOSs were not changed. In WT mice, fast IOSs could be observed at all ages from the OS and the amplitude and distribution did not show obvious changes over time [Fig. 5.2(A)]. In rd10 mouse, fast IOS image was similar to that of WT mouse at P15 [Fig. 5.2(B1)]. However, at P16 the amplitude of fast IOSs

decreased and fewer active pixels were observed [Fig. 5.2(B2)]. Fast IOSs in rd10 mice almost disappeared at P17 and totally disappeared afterwards [Fig. 5.2(B3) and (B4)]. Representative fast IOS curves showed the same amplitude changes as shown by IOS images as in Figures 5.2 (A) and (B). As shown in Figure 5.2(C1), amplitudes of fast IOSs in WT mice were similar at different ages, but as shown in Figure 5.2(C2), amplitudes of fast IOSs in rd10 mice decreased over time.
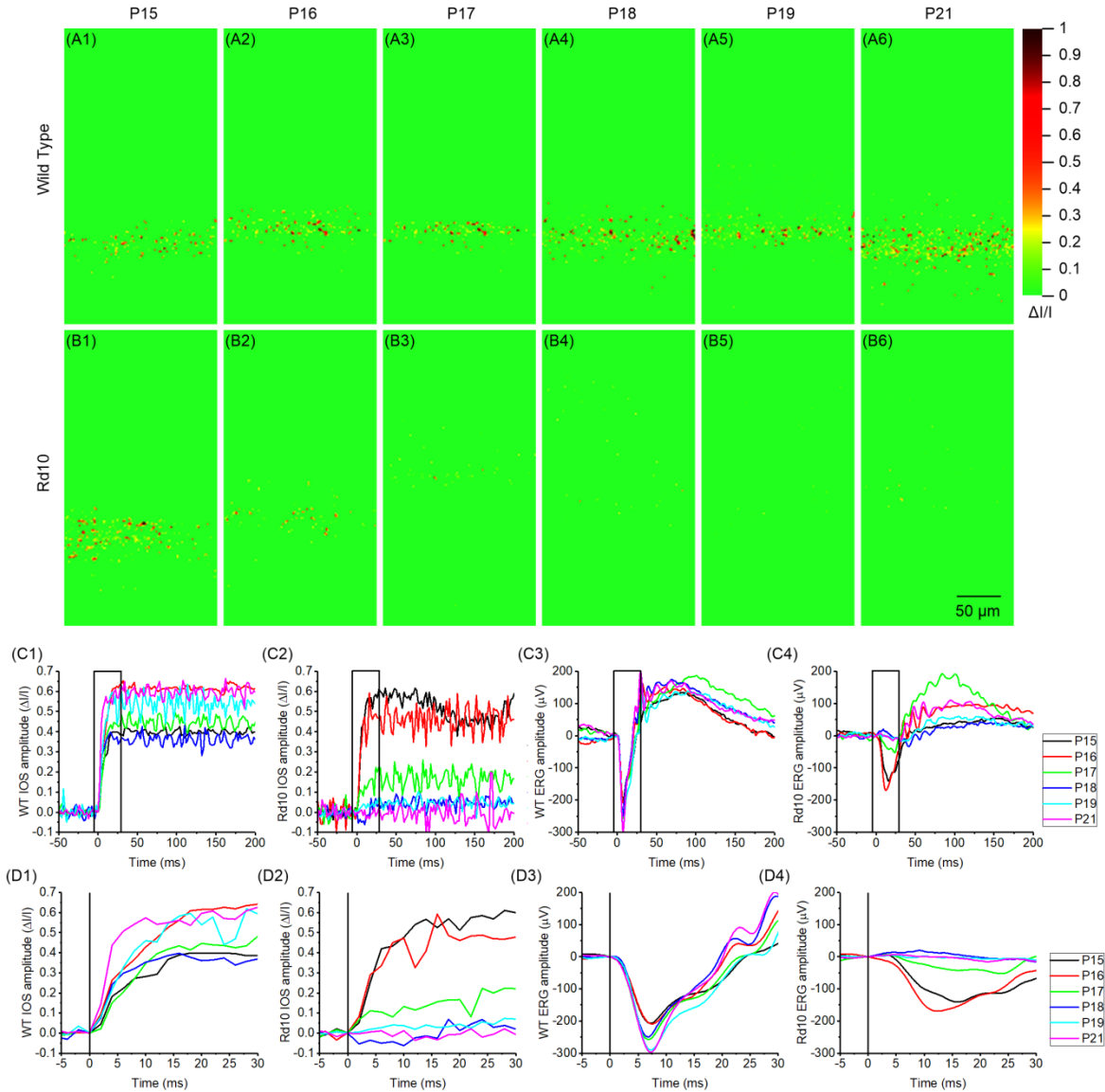
Fig. 5.2. Representative IOS images and ERGs observed in WT and rd10 mice from P15 to P21. (A) IOS images of WT mouse retinas from P15 to P21. (B) IOS images of rd10 mouse retinas from P15 to P21. (C) Fast IOSs of WT (C1) and rd10 (C2) mice at different ages, and ERG of WT (C3) and rd10 (C4) mice at different ages. (D) Enlarged view of black rectangle areas in C. D1-D4 correspond to C1-C4, respectively. Data shown were from different mice.

The ERG a-wave showed similar amplitude changes as in fast IOSs. In WT mice, the ERG a-wave amplitude showed no significant difference at different ages [Fig. 5.2 (C3)], while in rd10 mice, the amplitude decreased from P17, as shown in Figure 5.2 (C4). When looking more closely at the ERG a-wave of rd10 mice, as shown in Figure 5.2 (D4), the ERG a-wave was never normal. Even at P15, the ERG a-wave amplitude was smaller and the time-to-peak was longer comparing to WT mice [Fig. 5.2(D3)]. However, no obvious difference was observed in the fast IOS amplitude and time-to-peak at P15 between WT and rd10 mice, as shown in Figures 5.2 (D1) and (D2).

To further investigate the amplitudes and time courses of the ERG a-wave and fast IOSs, IOS imaging and ERG recording in both WT and rd10 mice were repeated multiple times. The ERG a-wave amplitude and time-to-peak, as well as the fast IOS amplitude and time-to-half-peak were calculated. Here, the fast IOS time-to-half-peak was used instead of the time-to-peak because, as shown in Figures 5.2 (D1) and (D2), it is hard to determine the first data point that reaches the peak of the fast IOS because of noise.
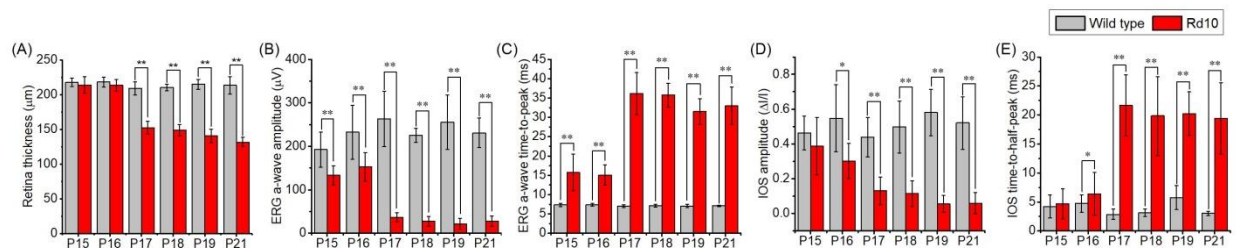
Fig. 5.3. Comparison between WT and rd10 mice of OCT, ERG, and IOS parameters at different ages. (A) Retina thickness changes of WT and rd10 mice at different ages. WT n=8, rd10 n=10. (B) ERG a-wave amplitude changes of WT and rd10 mice at different ages. N=6. (C) Fast IOS amplitude changes of WT and rd10 mice at different ages. N=6. (D) ERG a-wave time-to-peak changes of WT and rd10 mice at different ages. WT n=7, rd10 n=11. (E) Fast IOS time-to-half-peak changes of WT and rd10 mice at different ages. WT n=7, rd10 n=11. *: $p<0.05$; **: $p<0.01$.

Averaged results confirmed the observation in Figure 5.2. For WT mice, the ERG a-wave amplitude and time-to-peak did not show notable changes over time [Figs. 5.3(B) and (C)]. Similarly, no significant changes were observed for fast IOS amplitudes and time-to-half-peaks in WT mice [Figs. 5.3(D) and (E)]. For rd10 mice, ERG a-wave amplitudes did not change at P15 and P16, and rapidly

decreased from P17 [Fig. 5.3(B)]. The time-to-peak also did not change at P15 and P16, and rapidly increased from P17 [Fig. 5.3(C)]. Fast IOS amplitudes decreased gradually over time [Fig. 5.3(D)] and the time-to-half-peak increased from P17 [Fig. 5.3(E)].

When comparing WT and rd10 mice, it was observed that the amplitude and time-to-peak of ERG a-wave were already significantly different (p<0.01) from those of WT mice at P15 [Fig. 5.3(B) and (C)], when experiment started. The differences became more significant beginning from P17. For fast IOSs, statistically significant (p<0.05) differences between WT and rd10 mice were observed beginning from P16 using both amplitude [Fig. 5.3(D)] and time-to-half-peak [Fig. 5.3(E)] measurements. From P17, the significance level of the differences increased (p<0.01). For retina thickness, no statistically significant difference was observed at P15 and P16. From P17 the thickness difference became significant.

5.4 Discussion

In summary, functional OCT was used to evaluate fast IOS distortions and morphological abnormalities in rd10 mice aging from P15 to P21. Comparative electrophysiological measurements were conducted using full field ERGs. Statistically significant ERG, fast IOSs, and morphological differences between WT and rd10 mice were identified at P15, P16, and P17, respectively. The result that ERG and fast IOS identified difference between WT and rd10 mice earlier than OCT suggested that both ERG and fast IOS images were indicative of early retinal degeneration before statistically significant morphological changes could be identified.

At P16, there was no statistically significant thickness difference between WT and rd10 mice. However, there were some individuals that showed a thickness decrease at P16, and this observation agreed with a previous study [126]. The possible explanation that some individuals showed a thickness decrease while some did not at P16 is that, because the thickness decrease was rapid between P16 and P17 [Fig. 5.1(C)], the observation time point could affect the results. For example, an rd10 mouse

imaged at P16.5 might show a retinal thickness decrease even though its age was recorded as P16. The rapid thickness decrease, i.e., rapid photoreceptor death, between P16 and P17 could also explain the rapid amplitude and time-to-peak changes of ERG a-wave at P17 in rd10 mice observed in Figures 5.3 (B) and (C).

Although the ERG a-wave indicated retinal degeneration earlier than fast IOSs did, a limitation of an ERG is its low spatial resolution. Because ERG measures integrated electrical signals from the whole retina, it lacks spatial resolving capability and could not identify the location of retinal dysfunction. Even with multifocal ERG, the resolution is only ~5° (corresponding to ~2 mm in the human eye) [18, 19]. On the other hand, IOS imaging provides cellular resolution, such as 3 µm in this study, in both lateral and axial directions, making it easy to precisely identify the location and layer of the retina with dysfunction, so as to facilitate a more accurate and easier diagnosis.

The reason why fast IOSs showed distortion later than the ERG a-wave may be the limited sensitivity of our current OCT system. Due to eye movements introduced by the breath and heartbeat, movement noise was present in the fast IOSs and reduced IOS signal to noise ratio (SNR). However, the ERG was much less affected by eye movement and had a higher SNR than the fast IOSs. To improve the sensitivity of IOSs, an eye tracking system could be implemented into OCT to reduce movement noise [129, 130]. Another reason that fast IOS showed distortion later may reside in the different physiological originations of fast IOSs and ERG a-wave. ERG a-wave is generated by the last step of phototransduction process and PDE is involved in preceding steps. Thus, ERG a-wave is affected by reduced PDE activity in rd10 mice. However fast IOSs originate from early phototransduction process, and might not be affected by reduced PDE activity. According to our previous study, the fast IOSs onset time is as short as 0.4 ms [109], which is earlier than PDE activation [115], suggesting that fast IOSs might originate from phototransduction processes prior to PDE activation. Thus, at an early stage of retinal degeneration; i.e., P15, fast IOSs were observed as normal probably because early phototransduction processes were not affected by reduced PDE

activation. From P16 the accumulation of cGMP might have caused whole cell dysfunction that affected early steps of phototransduction. Thus, fast IOSs were observed with reduced amplitudes and elongated time courses beginning from P16.

In conclusion, comparative morphological OCT and functional fast IOS imaging of WT and rd10 mice was conducted. This study demonstrated the potential for using fast IOSs for early detection and progression monitoring of retinal photoreceptor degeneration. Further IOS study of rd10 and other mouse models could help provide a better understanding of disease-introduced IOS distortion and thus pave the way for clinical applications of high resolution IOS imaging to facilitate the early detection and diagnosis of retinal diseases.

Acknowledgments

CHAPTER VI. DISCUSSION AND CONCLUSION

In summary, characteristics of normal IOS in both isolated frog retinas and intact mouse retinas were studied. The physiological and dynamical mechanisms of fast IOS were explored. Fast IOS imaging in a diseased mouse model was conducted to test the potential of using fast IOS in clinical diagnosis of retinal diseases.

6.1 Characteristics of IOS

According to this dissertation research, the characteristics of IOS are listed as follows.

Spatial distribution: Positive and negative IOSs were mixed and confined in the stimulated area. Slow IOS was mainly observed in the inner retina with long stimulation (e.g. 500 ms) while rapid IOS was observed in photoreceptor OS with short stimulation (e.g. 10 ms).

Time scale: For fast IOS, negative IOS is slightly faster than positive IOS. Onset time is <3 ms for frogs and ~0.4 ms for mice. At ~20 ms after stimulus, fast IOS reaches the peak and stays at the peak for at least seconds. The time scales are affected by stimulation intensity.

Effect of stimulation intensity to fast IOS: The amplitude and time course changes of fast IOS in response to stimulation light intensity change are close to the change of ERG a-wave, i.e., as stimulation intensity increases, amplitude increases, onset time and peak time get shorter.

Effect of retinal disease to fast IOS: In retina with dysfunction, the amplitude of fast IOS decreased and time course increased. Fast IOS was capable of detecting retinal dysfunction in rd10 mouse one day earlier than OCT.

Mechanism: Dynamically, one main origination of fast IOS is the phototropism observed in rods. Physiologically, fast IOS originated from early phototransduction process.

From all our studies using different imaging modalities including line scan confocal microscopy, LS-OCT and SD-OCT, positive and negative pixels were mixed together in IOS images. This suggests that it is a good practice to process positive and negative pixels separately to achieve maximum signal sensitivity. Because if positive and negative pixels are not separated and are averaged together, they could cancel each other and significantly decrease IOS amplitude [1]. To ensure successful separation of positive and negative pixels, resolution of the imaging system should reach cellular level, because the process that generates IOS signal is within each individual photoreceptor cell.

Chapter V shows that the two biomarkers, time course and amplitude of fast IOS, could be used for diagnosing retinal dysfunction. To use the time course as a diagnosing biomarker, high imaging speed is necessary because fast IOS has millisecond level time courses. To accurately capture the onset time and peak time in fast IOS imaging, imaging speed higher than 500 frames per second is preferable. However, if imaging speed is limited and peak time could not be accurately measured, fast IOS amplitude could always be a biomarker for evaluating retinal dysfunction since measuring the amplitude of fast IOS does not require such high speed.

6.2 Mechanism of fast IOS

Dynamical mechanism of fast IOS was studied in Chapter III. Phototransduction was found to be the main dynamical origination of IOS observed in photoreceptor OS. When a photoreceptor cell moves, the movement causes pixel intensity changes in recorded images. For example, when a bright spot moves, the pixels that the bright spot moves to gets brighter and the pixels that the bright spot moved away from gets darker, then positive and negative IOSs are observed. The mechanism of photoreceptor movement is not clear yet. More studies have been conducted after the study in Chapter III. Using wide-field microscope, rod OS movement upon oblique stimulus was clearly observed in retinal slices [108]. We suspected that the movement

was caused by unbalanced illumination on two sides of the photoreceptor which caused unbalanced intra-disc or inter-disc space change, then caused photoreceptor to bend. By shining light only on a half side of the OS, OS was observed to bend toward the illuminated side [108]. This suggested that the illuminated side shrank. In a recent study, OS was imaged under electron microscope (EM), the inter-disc distance was observed decreased after the rod was exposed to light. The physiological reason that causes inter-disc distance reduction is not clear yet.

Physiological mechanism of fast IOS was explored in both Chapter II and Chapter IV. Phototropism is not the only contributor to fast IOS, because if fast IOS only results from OS movement, the time courses of positive and negative fast IOSs should be the same. However, negative fast IOS was observed faster than positive fast IOS. Thus, some physiological process also caused the light property changes of the photoreceptors. In Chapter IV we concluded that fast IOS may originate from early phototransduction process. This conclusion agrees with our inference in Chapter II, that fast IOS may be originated from G-protein binding and releasing process in phototransduction. A physiological study was conducted by a colleague to test the physiological origination of fast IOS and phototropism [122]. In that study, the isolated frog retina was imaged under a wide-field microscope. When stimulated with visible light, fast IOS and phototropism, as well as ERG a-wave were observed. However, when the solution that the isolated retina resided in was replaced with low Na^+ solution, ERG a-wave disappeared while phototropism and fast IOS remained present. When the solution was changed back to normal solution, ERG a-wave came back and phototropism and fast IOS were still present. This study provided direct evidence that fast IOS and phototropism originated from early phototransduction process before the hyperpolarization of the photoreceptor cell.

This dissertation research was not specifically designed to study the different contribution of rod and cones to fast IOS, all samples were dark adapted thus observed results reflected mainly rod

activity. Photoreceptor phototropism was the main contributor to fast IOS. It was observed that phototropism was mainly observed in rods [74], this agrees with the IOS observation that fast IOS was mainly observed in dark adapted retinas (Fig. 4.3), and in light adapted retinas the IOS was very small (Fig. 4.4) in amplitude. We could conclude that fast IOS was mainly contributed by rod phototropism, and rod phototransduction. The contribution of cones to fast IOS was smaller but still detectable. One reason that the IOS observed in Figure 4.4 was so small in amplitude may be that the ratio of cones in mouse retinas is small, only ~3% of all photoreceptor cells. In frog retinas, where the ratio of cones is ~50%, more significant IOS was observed in light adapted retinas [16]. It would be interesting to specifically study how IOSs from rods and cones are different. It was observed that light adapted ERG showed smaller amplitude and faster kinetics than dark adapted ERG. Similarly, we could expect light adapted IOS to have smaller amplitude and faster kinetics.

Currently, we are only able to narrow down the origination of fast IOS to phototransduction before cell hyperpolarization. Further study that uses different chemicals to block certain step or steps of phototransduction could help narrow down the physiological origination of fast IOS to a specific phototransduction step and help us understand fast IOS better. Another study that could be conducted to study the mechanism is to record IOS from multiple flash stimuli. By stimulating isolated bovine retina with two flashes of certain intensity, Dr. Pepperberg $et.$ $al.$ observed an inverse exponential relationship between A_2/A_1 and t_I. A_1 and A_2 are scattering light intensity changes induced by the first and second flashes, respectively. t_I is the inter-flash interval [128]. The observed scattering light intensity change was contributed to activated rhodopsin R*-catalyzed and disc-localized reaction of phototransduction. If same relationship could be observed, i.e. there is inverse exponential relationship between IOS_2/IOS_1 and t_I, it would suggest that the IOS observed in this dissertation research shares same mechanism as the scattering light change observed by Dr. Pepperberg. Such study would be challenging because

the amplitude of the second IOS would be significantly smaller than the first one, thus high imaging sensitivity is required to reliably detect the second IOS. It would be much easier to conduct such a study using isolated retina tissue since there is essentially no movement noise thus imaging sensitivity would be high.

6.3 Future direction and clinical application

Before applying IOS in clinic, more studies using diseased animal models are favorable so that we could understand how different diseases alter IOS. In Chapter V a study using an RP mouse model (rd10 mouse) was demonstrated, and more study could be done using this model. For example, it is known that in the rd10 mouse model the retina degeneration in the peripheral retina is slower than that in the central retina [131], thus it would be interesting to image a larger area that covers both central and peripheral retina and fast IOS from different areas could be compared. ERG is not capable of such study because it lacks spatial resolving capability. One challenge in large field-of-view IOS imaging is that imaging speed must be sacrificed in order to increase the field of view. However, because of the eye movement, the imaging speed should be relatively high otherwise the eye movement will blur the image. Thus, faster camera will be necessary for such study. Besides the rd10 mouse model, there are other diseased models, for example, non-obese diabetic mice for studying type 1 diabetes, the db/db (*Lepr*^{db}) mouse for studying type 2 diabetes, etc.

In vivo fast IOS imaging in human is challenging because of the fixational eye movement. The fixational eye movement is involuntary movement when eyes are fixed at target. For example, Microtremors, one form of fixational eye movement that has an amplitude close to photoreceptor diameter, and frequency of 40-100 Hz [132], could significantly affect the recording of fast IOS because of its high frequency and relatively large amplitude comparing to the size of photoreceptor cells. If image registration is to be used for removing microtremors, imaging

speed should be much higher than 100 Hz, for example, 500 Hz. Another way to remove fixational eye movement is to integrate eye tracking into the imaging system. Eye tracking has been implemented into OCT and was proved to be effective in stabilizing retinal image [129, 130]. If eye tracking was to be integrated into IOS imaging, it could significantly improve IOS SNR and sensitivity.

Different imaging modalities could be used for IOS imaging in clinic, such as OCT, line-scan confocal microscopy, and fundus camera. OCT provides high-resolution layered structure of the retina that is useful for diagnosis, thus is widely used in eye clinic. In my dissertation research, OCT was selected as the imaging device because we could selectively focus on one layer, e.g. OS, and don't need to worry about signal crosstalk. However, one problem of IOS imaging using OCT also arises from its high axial resolution. For both TD-OCT and SD-OCT, eye movement in imaging plane could be effectively removed by image registration, given that imaging speed is sufficient. But eye movement perpendicular to imaging plane could not be removed by image registration. To solve this problem, in situations where the layered structure of the retina provides important information, eye tracking should be integrated into OCT to reduce eye movement. In other situations where layered structure information is not important, line-scan confocal microscope could be the better imaging modality. Line-scan confocal microscope provides high lateral resolution for IOS imaging, and lower axial resolution than OCT to tolerant eye movement in axial direction.

In conclusion, this dissertation study improved our understanding of IOS regarding its characteristics, mechanism and relationship with retina diseases. The feasibility of using fast IOS as a tool for retinal disease diagnosis was demonstrated. Further studies are necessary to reveal the physiological mechanism of IOS and how different retinal diseases affect IOS in more depth. With the development of camera technology, high speed and high sensitivity cameras will be available. We could ultimately build a high speed large field IOS imager with eye tracking

integrated. Such IOS imager will be a powerful tool in clinic that provides both high resolution morphological and functional images of the retina to help with early diagnosis and treatment evaluation of retinal diseases.

CITED LITERATURE

1. Wang, B., et al., *En face optical coherence tomography of transient light response at photoreceptor outer segments in living frog eyecup.* Opt Lett, 2013. **38**(22): p. 4526-9.

2. Wang, B., et al., *Functional optical coherence tomography reveals transient phototropic change of photoreceptor outer segments.* Opt Lett, 2014. **39**(24): p. 6923-6.

3. Wang, B., Y. Lu, and X. Yao, *In vivo optical coherence tomography of stimulus-evoked intrinsic optical signals in mouse retinas.* J Biomed Opt, 2016. **21**(9): p. 96010.

4. Curcio, C.A., N.E. Medeiros, and C.L. Millican, *Photoreceptor loss in age-related macular degeneration.* Invest Ophthalmol Vis Sci, 1996. **37**(7): p. 1236-49.

5. Owsley, C., et al., *Cone- and rod-mediated dark adaptation impairment in age-related maculopathy.* Ophthalmology, 2007. **114**(9): p. 1728-35.

6. Nagy, D., et al., *Long-term follow-up of retinitis pigmentosa patients with multifocal electroretinography.* Invest Ophthalmol Vis Sci, 2008. **49**(10): p. 4664-71.

7. Qin, Y., G. Xu, and W. Wang, *Dendritic abnormalities in retinal ganglion cells of three-month diabetic rats.* Curr Eye Res, 2006. **31**(11): p. 967-74.

8. Meyer-Rusenberg, B., et al., *Pathological changes in human retinal ganglion cells associated with diabetic and hypertensive retinopathy.* Graefes Arch Clin Exp Ophthalmol, 2007. **245**(7): p. 1009-18.

9. Harwerth, R.S. and H.A. Quigley, *Visual field defects and retinal ganglion cell losses in patients with glaucoma.* Arch Ophthalmol, 2006. **124**(6): p. 853-9.

10. Nickells, R.W., *Ganglion cell death in glaucoma: from mice to men.* Vet Ophthalmol, 2007. **10 Suppl 1**: p. 88-94.

11. Scholl, H.P. and E. Zrenner, *Electrophysiology in the investigation of acquired retinal disorders.* Surv Ophthalmol, 2000. **45**(1): p. 29-47.

12. Zhang, Q.X., et al., *In vivo confocal imaging of fast intrinsic optical signals correlated with frog retinal activation.* Opt Lett, 2011. **36**(23): p. 4692-4.

13. Yao, X.C. and Y.C. Li, *Functional imaging of retinal photoreceptors and inner neurons using stimulus-evoked intrinsic optical signals.* Methods Mol Biol, 2012. **884**: p. 277-85.

14. Zhang, Q.X., et al., *In vivo confocal intrinsic optical signal identification of localized retinal dysfunction.* Invest Ophthalmol Vis Sci, 2012. **53**(13): p. 8139-45.

15. Li, Y.C., et al., *Parallel optical monitoring of visual signal propagation from the photoreceptors to the inner retina layers.* Opt Lett, 2010. **35**(11): p. 1810-2.

16. Zhang, Q., et al., *Functional optical coherence tomography enables in vivo physiological assessment of retinal rod and cone photoreceptors.* Sci Rep, 2015. **5**: p. 9595.

17.   Puliafito, C.A., et al., *Imaging of macular diseases with optical coherence tomography.* Ophthalmology, 1995. **102**(2): p. 217-29.

18.   Ball, S.L. and H.M. Petry, *Noninvasive assessment of retinal function in rats using multifocal electroretinography.* Invest Ophthalmol Vis Sci, 2000. **41**(2): p. 610-7.

19.   Hood, D.C., *Assessing retinal function with the multifocal technique.* Prog Retin Eye Res, 2000. **19**(5): p. 607-46.

20.   Kolb, H., *Gross Anatomy of the Eye by Helga Kolb.* Webvision, 2017.

21.   Kolb, H., *Simple Anatomy of the Retina by Helga Kolb.* Webvision, 2017.

22.   Jmarchn, *Cone rode ca.* 2014, Wikimedia Commons.

23.   Dowling, J.E., *Two: Retinal cells and informationa processing*, in *The retina: an approachable part of the brain*. 1987, Belknap Press of Harvard University Press.

24.   Curcio, C.A., et al., *Human photoreceptor topography.* J Comp Neurol, 1990. **292**(4): p. 497-523.

25.   Schnapf, J.L., T.W. Kraft, and D.A. Baylor, *Spectral sensitivity of human cone photoreceptors.* Nature, 1987. **325**(6103): p. 439-41.

26.   Pennesi, M.E., et al., *Long-term characterization of retinal degeneration in rd1 and rd10 mice using spectral domain optical coherence tomography.* Invest Ophthalmol Vis Sci, 2012. **53**(8): p. 4644-56.

27.   Corneveaux, J.J., *Phototransduction.* 2007, Wikimedia Commons.

28.   Pugh, E.N., Jr. and T.D. Lamb, *Amplification and kinetics of the activation steps in phototransduction.* Biochim Biophys Acta, 1993. **1141**(2-3): p. 111-49.

29.   Lagnado, L. and D. Baylor, *Signal flow in visual transduction.* Neuron, 1992. **8**(6): p. 995-1002.

30.   Chen, C.K., *The vertebrate phototransduction cascade: amplification and termination mechanisms.* Rev Physiol Biochem Pharmacol, 2005. **154**: p. 101-21.

31.   Schoenlein, R.W., et al., *The first step in vision: femtosecond isomerization of rhodopsin.* Science, 1991. **254**(5030): p. 412-5.

32.   Lewis, J.W. and D.S. Kliger, *Photointermediates of visual pigments.* J Bioenerg Biomembr, 1992. **24**(2): p. 201-10.

33.   Preininger, A.M. and H.E. Hamm, *G protein signaling: insights from new structures.* Sci STKE, 2004. **2004**(218): p. re3.

34.   Kaupp, U.B., et al., *Electrical and biochemical properties of the cGMP-gated cation channel from rod photoreceptors.* Cold Spring Harb Symp Quant Biol, 1988. **53 Pt 1**: p. 407-15.

35. Einthoven, W. and W.A. Jolly, *THE FORM AND MAGNITUDE OF THE ELECTRICAL RESPONSE OF THE EYE TO STIMULATION BY LIGHT AT VARIOUS INTENSITIES.* Quarterly Journal of Experimental Physiology, 1908. **1**(4): p. 373-416.

36. Hood, D.C., et al., *Assessment of local retinal function in patients with retinitis pigmentosa using the multi-focal ERG technique.* Vision Res, 1998. **38**(1): p. 163-79.

37. Seeliger, M., et al., *Multifocal electroretinography in retinitis pigmentosa.* Am J Ophthalmol, 1998. **125**(2): p. 214-26.

38. Lachapelle, P., J.M. Little, and R.C. Polomeno, *The photopic electroretinogram in congenital stationary night blindness with myopia.* Invest Ophthalmol Vis Sci, 1983. **24**(4): p. 442-50.

39. Miyake, Y., et al., *Congenital stationary night blindness with negative electroretinogram. A new classification.* Arch Ophthalmol, 1986. **104**(7): p. 1013-20.

40. Creel, D.J., *The Electroretinogram and Electro-oculogram: Clinical Applications.* Webvision, 2017.

41. Penn, R.D. and W.A. Hagins, *Signal transmission along retinal rods and the origin of the electroretinographic a-wave.* Nature, 1969. **223**(5202): p. 201-4.

42. Sillman, A.J., H. Ito, and T. Tomita, *Studies on the mass receptor potential of the isolated frog retina. II. On the basis of the ionic mechanism.* Vision Res, 1969. **9**(12): p. 1443-51.

43. Dick, E. and R.F. Miller, *Extracellular K+ activity changes related to electroretinogram components. I. Amphibian (I-type) retinas.* J Gen Physiol, 1985. **85**(6): p. 885-909.

44. Dick, E., R.F. Miller, and S. Bloomfield, *Extracellular K+ activity changes related to electroretinogram components. II. Rabbit (E-type) retinas.* J Gen Physiol, 1985. **85**(6): p. 911-31.

45. Karowski, C.J. and L.M. Proenza, *Relationship between Muller cell responses, a local transretinal potential, and potassium flux.* J Neurophysiol, 1977. **40**(2): p. 244-59.

46. Newman, E.A., *Current source-density analysis of the b-wave of frog retina.* J Neurophysiol, 1980. **43**(5): p. 1355-66.

47. Miller, R.F. and J.E. Dowling, *Intracellular responses of the Muller (glial) cells of mudpuppy retina: their relation to b-wave of the electroretinogram.* J Neurophysiol, 1970. **33**(3): p. 323-41.

48. Oakley, B., 2nd and D.G. Green, *Correlation of light-induced changes in retinal extracellular potassium concentration with c-wave of the electroretinogram.* J Neurophysiol, 1976. **39**(5): p. 1117-33.

49. Oakley, B., 2nd, *Potassium and the photoreceptor-dependent pigment epithelial hyperpolarization.* J Gen Physiol, 1977. **70**(4): p. 405-25.

50.   Huang, D., et al., *Optical coherence tomography.* Science, 1991. **254**(5035): p. 1178-81.

51.   Fung, A.E., et al., *An optical coherence tomography-guided, variable dosing regimen with intravitreal ranibizumab (Lucentis) for neovascular age-related macular degeneration.* Am J Ophthalmol, 2007. **143**(4): p. 566-83.

52.   Lalwani, G.A., et al., *A variable-dosing regimen with intravitreal ranibizumab for neovascular age-related macular degeneration: year 2 of the PrONTO Study.* Am J Ophthalmol, 2009. **148**(1): p. 43-58 e1.

53.   Hirakawa, H., et al., *Optical coherence tomography of cystoid macular edema associated with retinitis pigmentosa.* Am J Ophthalmol, 1999. **128**(2): p. 185-91.

54.   Hagiwara, A., et al., *Macular abnormalities in patients with retinitis pigmentosa: prevalence on OCT examination and outcomes of vitreoretinal surgery.* Acta Ophthalmologica, 2011. **89**(2): p. E122-E125.

55.   Choma, M., et al., *Sensitivity advantage of swept source and Fourier domain optical coherence tomography.* Opt Express, 2003. **11**(18): p. 2183-9.

56.   Leitgeb, R., C. Hitzenberger, and A. Fercher, *Performance of fourier domain vs. time domain optical coherence tomography.* Opt Express, 2003. **11**(8): p. 889-94.

57.   Yao, X. and B. Wang, *Intrinsic optical signal imaging of retinal physiology: a review.* J Biomed Opt, 2015. **20**(9): p. 90901.

58.   Bennett, N., *Light-Induced Interactions between Rhodopsin and the Gtp-Binding Protein - Relation with Phosphodiesterase Activation.* European Journal of Biochemistry, 1982. **123**(1): p. 133-139.

59.   Son, T., et al., *Optical coherence tomography angiography of stimulus evoked hemodynamic responses in individual retinal layers.* Biomedical Optics Express, 2016. **7**(8): p. 3151-3162.

60.   Zhang, Q.X., et al., *Microlens array recording of localized retinal responses.* Opt Lett, 2010. **35**(22): p. 3838-40.

61.   Li, Y.G., et al., *High spatiotemporal resolution imaging of fast intrinsic optical signals activated by retinal flicker stimulation.* Opt Express, 2010. **18**(7): p. 7210-8.

62.   Li, Y.G., et al., *High-speed line-scan confocal imaging of stimulus-evoked intrinsic optical signals in the retina.* Opt Lett, 2010. **35**(3): p. 426-8.

63.   Yao, X.C., *Intrinsic optical signal imaging of retinal activation.* Jpn J Ophthalmol, 2009. **53**(4): p. 327-33.

64.   Moayed, A.A., et al., *In vivo imaging of intrinsic optical signals in chicken retina with functional optical coherence tomography.* Opt Lett, 2011. **36**(23): p. 4575-7.

65.   Akhlagh Moayed, A., et al., *Correlation of visually evoked intrinsic optical signals and electroretinograms recorded from chicken retina with a combined functional optical*

coherence tomography and electroretinography system. J Biomed Opt, 2012. **17**(1): p. 016011.

66.   Srinivasan, V.J., et al., *In vivo measurement of retinal physiology with high-speed ultrahigh-resolution optical coherence tomography.* Opt Lett, 2006. **31**(15): p. 2308-10.

67.   Bizheva, K., et al., *Optophysiology: depth-resolved probing of retinal physiology with functional ultrahigh-resolution optical coherence tomography.* Proc Natl Acad Sci U S A, 2006. **103**(13): p. 5066-71.

68.   Ts'o, D., et al., *Noninvasive functional imaging of the retina reveals outer retinal and hemodynamic intrinsic optical signal origins.* Jpn J Ophthalmol, 2009. **53**(4): p. 334-44.

69.   Hanazono, G., et al., *Intrinsic signal imaging in macaque retina reveals different types of flash-induced light reflectance changes of different origins.* Invest Ophthalmol Vis Sci, 2007. **48**(6): p. 2903-12.

70.   Srinivasan, V.J., et al., *In vivo functional imaging of intrinsic scattering changes in the human retina with high-speed ultrahigh resolution OCT.* Opt Express, 2009. **17**(5): p. 3861-77.

71.   Abramoff, M.D., et al., *Visual stimulus-induced changes in human near-infrared fundus reflectance.* Invest Ophthalmol Vis Sci, 2006. **47**(2): p. 715-21.

72.   Hillmann, D., et al., *In vivo optical imaging of physiological responses to photostimulation in human photoreceptors.* Proc Natl Acad Sci U S A, 2016. **113**(46): p. 13138-13143.

73.   Zhang, Q.X., et al., *Comparative intrinsic optical signal imaging of wild-type and mutant mouse retinas.* Opt Express, 2012. **20**(7): p. 7646-54.

74.   Lu, R., et al., *Dynamic near-infrared imaging reveals transient phototropic change in retinal rod photoreceptors.* J Biomed Opt, 2013. **18**(10): p. 106013.

75.   Sunness, J.S., et al., *Diminished foveal sensitivity may predict the development of advanced age-related macular degeneration.* Ophthalmology, 1989. **96**(3): p. 375-81.

76.   Quigley, H.A., E.M. Addicks, and W.R. Green, *Optic nerve damage in human glaucoma. III. Quantitative correlation of nerve fiber loss and visual field defect in glaucoma, ischemic neuropathy, papilledema, and toxic neuropathy.* Arch Ophthalmol, 1982. **100**(1): p. 135-46.

77.   Jacobson, S.G., et al., *Disease expression of RP1 mutations causing autosomal dominant retinitis pigmentosa.* Invest Ophthalmol Vis Sci, 2000. **41**(7): p. 1898-908.

78.   Johnson, P.T., et al., *Drusen-associated degeneration in the retina.* Invest Ophthalmol Vis Sci, 2003. **44**(10): p. 4481-8.

79.   Hogg, R.E. and U. Chakravarthy, *Visual function and dysfunction in early and late age-related maculopathy.* Prog Retin Eye Res, 2006. **25**(3): p. 249-76.

80. Yao, X.C., D.M. Rector, and J.S. George, *Optical lever recording of displacements from activated lobster nerve bundles and Nitella internodes.* Appl Opt, 2003. **42**(16): p. 2972-8.

81. Yao, X.C., et al., *Cross-polarized reflected light measurement of fast optical responses associated with neural activation.* Biophys J, 2005. **88**(6): p. 4170-7.

82. Schei, J.L., et al., *Action potential propagation imaged with high temporal resolution near-infrared video microscopy and polarized light.* Neuroimage, 2008. **40**(3): p. 1034-1043.

83. Lu, R.W., Q.X. Zhang, and X.C. Yao, *Circular polarization intrinsic optical signal recording of stimulus-evoked neural activity.* Opt Lett, 2011. **36**(10): p. 1866-8.

84. Li, Y.C., et al., *Intrinsic optical signal imaging of glucose-stimulated insulin secreting beta-cells.* Opt Express, 2011. **19**(1): p. 99-106.

85. Yao, X.C., et al., *Functional imaging of glucose-evoked rat islet activities using transient intrinsic optical signals.* Journal of Modern Optics, 2012. **59**(7): p. 843-847.

86. Schallek, J., et al., *Stimulus-evoked intrinsic optical signals in the retina: spatial and temporal characteristics.* Invest Ophthalmol Vis Sci, 2009. **50**(10): p. 4865-72.

87. Jonnal, R.S., et al., *In vivo functional imaging of human cone photoreceptors.* Optics Express, 2007. **15**(24): p. 16141-16160.

88. Grieve, K. and A. Roorda, *Intrinsic signals from human cone photoreceptors.* Invest Ophthalmol Vis Sci, 2008. **49**(2): p. 713-9.

89. Rha, J., et al., *Variable optical activation of human cone photoreceptors visualized using a short coherence light source.* Optics Letters, 2009. **34**(24): p. 3782-3784.

90. Yao, X.C., et al., *Rapid optical coherence tomography and recording functional scattering changes from activated frog retina.* Applied Optics, 2005. **44**(11): p. 2019-2023.

91. Lu, R.W., et al., *Investigation of the hyper-reflective inner/outer segment band in optical coherence tomography of living frog retina.* J Biomed Opt, 2012. **17**(6): p. 060504.

92. Hofmann, K.P., et al., *Measurements on fast light-induced light-scattering and -absorption changes in outer segments of vertebrate light sensitive rod cells.* Biophys Struct Mech, 1976. **2**(1): p. 61-77.

93. Kuhn, H., et al., *Interactions between photoexcited rhodopsin and GTP-binding protein: kinetic and stoichiometric analyses from light-scattering changes.* Proc Natl Acad Sci U S A, 1981. **78**(11): p. 6873-7.

94. Arshavsky, V.Y., T.D. Lamb, and E.N. Pugh, Jr., *G proteins and phototransduction.* Annu Rev Physiol, 2002. **64**: p. 153-87.

95. Stiles, W.S. and B.H. Crawford, *The luminous efficiency of rays entering the eye pupil at different points.* Proceedings royal society of London, 1933. **112**(778): p. 428-450.

96.   Westheimer, G., *Directional sensitivity of the retina: 75 years of Stiles-Crawford effect.* Proc Biol Sci, 2008. **275**(1653): p. 2777-86.

97.   Packer, O.S., D.R. Williams, and D.G. Bensinger, *Photopigment transmittance imaging of the primate photoreceptor mosaic.* J Neurosci, 1996. **16**(7): p. 2251-60.

98.   Vohnsen, B., I. Iglesias, and P. Artal, *Guided light and diffraction model of human-eye photoreceptors.* J Opt Soc Am A Opt Image Sci Vis, 2005. **22**(11): p. 2318-28.

99.   Rativa, D. and B. Vohnsen, *Simulating human photoreceptor optics using a liquid-filled photonic crystal fiber.* Biomedical Optics Express, 2011. **2**(3): p. 543-551.

100.   Zhang, Q.X., et al., *In vivo Optical Coherence Tomography of Light-Driven Melanosome Translocation in Retinal Pigment Epithelium.* Sci Rep, 2013. **3**: p. 2644.

101.   Nilsson, S.E., *An Electron Microscopic Classification of the Retinal Receptors of the Leopard Frog (Rana Pipiens).* J Ultrastruct Res, 1964. **10**: p. 390-416.

102.   Liebman, P.A. and G. Entine, *Visual pigments of frog and tadpole (Rana pipiens).* Vision Res, 1968. **8**(7): p. 761-75.

103.   Yao, X.C. and Y.B. Zhao, *Optical dissection of stimulus-evoked retinal activation.* Opt Express, 2008. **16**(17): p. 12446-59.

104.   Deqing, S., S. Roth, and M.J. Black. *Secrets of optical flow estimation and their principles.* in *Computer Vision and Pattern Recognition (CVPR), 2010 IEEE Conference.* 2010.

105.   Otsu, N., *A threshold selection method from gray-level histograms.* Automatica, 1975. **11**(285-296): p. 23-27.

106.   Schmitt, J.M., S.H. Xiang, and K.M. Yung, *Speckle in optical coherence tomography.* J Biomed Opt, 1999. **4**(1): p. 95-105.

107.   Yao, X.C. and J.S. George, *Near-infrared imaging of fast intrinsic optical responses in visible light-activated amphibian retina.* J Biomed Opt, 2006. **11**(6): p. 064030.

108.   Zhao, X., et al., *Stimulus-evoked outer segment changes in rod photoreceptors.* J Biomed Opt, 2016. **21**(6): p. 65006.

109.   Wang, B. and X. Yao. *In vivo intrinsic optical signal imaging of mouse retinas.* 2016.

110.   Paxinos, G., et al., *Bregma, lambda and the interaural midpoint in stereotaxic surgery with rats of different sex, strain and weight.* J Neurosci Methods, 1985. **13**(2): p. 139-43.

111.   Geiger, B.M., et al., *Survivable stereotaxic surgery in rodents.* J Vis Exp, 2008(20).

112.   Liu, X., et al., *Effect of contact lens on optical coherence tomography imaging of rodent retina.* Curr Eye Res, 2013. **38**(12): p. 1235-40.

113.   Hamasaki, D.I., et al., *The a-wave latency in control subjects and patients with retinal diseases.* Jpn J Ophthalmol, 2002. **46**(4): p. 433-42.

114. Strauss, O., *The Retinal Pigment Epithelium in Visual Function.* Physiological Reviews, 2005. **85**(3): p. 845-881.

115. Yoshizawa, T. and H. Kandori, *Primary photochemical events in the rhodopsin molecule.* Progress in retinal research, 1991. **11**: p. 33-55.

116. Fu, Y. and K.W. Yau, *Phototransduction in mouse rods and cones.* Pflugers Arch, 2007. **454**(5): p. 805-19.

117. Klein, R., et al., *Diabetic retinopathy as detected using ophthalmoscopy, a nonmydriatic camera and a standard fundus camera.* Ophthalmology, 1985. **92**(4): p. 485-91.

118. Toslak, D., et al., *Trans-palpebral illumination: an approach for wide-angle fundus photography without the need for pupil dilation.* Opt Lett, 2016. **41**(12): p. 2688-91.

119. Webb, R.H. and G.W. Hughes, *Scanning laser ophthalmoscope.* IEEE Trans Biomed Eng, 1981. **28**(7): p. 488-92.

120. Investigators, A.G.I.S., *Advanced Glaucoma Intervention Study. 2. Visual field test scoring and reliability.* Ophthalmology, 1994. **101**(8): p. 1445-55.

121. Naderian, A., et al., *Cellular origin of intrinsic optical signals in the rabbit retina.* Vision Res, 2017. **137**: p. 40-49.

122. Lu, Y., et al., *Stimulus-evoked outer segment changes occur before the hyperpolarization of retinal photoreceptors.* Biomed Opt Express, 2017. **8**(1): p. 38-47.

123. Chang, B., et al., *Two mouse retinal degenerations caused by missense mutations in the beta-subunit of rod cGMP phosphodiesterase gene.* Vision Res, 2007. **47**(5): p. 624-33.

124. Bowes, C., et al., *Retinal degeneration in the rd mouse is caused by a defect in the beta subunit of rod cGMP-phosphodiesterase.* Nature, 1990. **347**(6294): p. 677-80.

125. Stockman, A., D.I. MacLeod, and N.E. Johnson, *Spectral sensitivities of the human cones.* J Opt Soc Am A Opt Image Sci Vis, 1993. **10**(12): p. 2491-521.

126. Chang, B., et al., *Retinal degeneration mutants in the mouse.* Vision Res, 2002. **42**(4): p. 517-25.

127. *Ophthalmic instruments-Fundamental requirements and test methods*, in *ISO 15004-2.* 2007, International Organization for Standardization.

128. Pepperberg, D.R., et al., *Photic modulation of a highly sensitive, near-infrared light-scattering signal recorded from intact retinal photoreceptors.* Proc Natl Acad Sci U S A, 1988. **85**(15): p. 5531-5.

129. Vienola, K.V., et al., *Real-time eye motion compensation for OCT imaging with tracking SLO.* Biomed Opt Express, 2012. **3**(11): p. 2950-63.

130. Braaf, B., et al., *Real-time eye motion correction in phase-resolved OCT angiography with tracking SLO.* Biomed Opt Express, 2013. **4**(1): p. 51-65.

131.   Gargini, C., et al., *Retinal organization in the retinal degeneration 10 (rd10) mutant mouse: a morphological and ERG study.* J Comp Neurol, 2007. **500**(2): p. 222-38.

132.   Martinez-Conde, S., S.L. Macknik, and D.H. Hubel, *The role of fixational eye movements in visual perception.* Nat Rev Neurosci, 2004. **5**(3): p. 229-40.

APPENDICES

ACC approval

UIC UNIVERSITY OF ILLINOIS AT CHICAGO

March 3, 2015

Office of Animal Care and
Institutional Biosafety Committees (MC 672)
Office of the Vice Chancellor for Research
206 Administrative Office Building
1737 West Polk Street
Chicago, Illinois 60612-7227

Xincheng Yao
Bioengineering
M/C 063

Dear Dr. Yao:

The protocol indicated below was reviewed at a convened ACC meeting in accordance with the Animal Care Policies of the University of Illinois at Chicago on **12/16/2014**. *The protocol was not initiated until final clarifications were reviewed and approved on* **2/27/2015**. *The protocol is approved for a period of* **3** *years with annual continuation.*

Title of Application: Intrinsic Optical Signal Imaging of Retinal Function

ACC Number: 14-201

Initial Approval Period: 2/27/2015 to 12/16/2015

Current Funding: <mark>*Portions of this protocol are supported by the funding sources indicated in the table below.*</mark>
Number of funding sources: 3
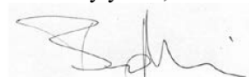
Funding Agency	Funding Title			Portion of Proposal Matched
NIH	*Functional Imaging of Retinal Photoreceptors*			*All matched*
Funding Number	**Current Status**	**UIC PAF NO.**	**Performance Site**	**Funding PI**
RO1 EY023522 (years 1-5)	*Pending*	*201503177*	*UIC*	*Xincheng Yao*
Funding Agency	**Funding Title**			**Portion of Proposal Matched**
NIH	*Super-Resulation Ophtaalmoscopy for in Vivo Rential Imaging*			*All matched*
Funding Number	**Current Status**	**UIC PAF NO.**	**Performance Site**	**Funding PI**
RO1 EY024628 (years 1-3)	*Pending*	*201503176*	*UIC*	*Xincheng Yao*
Funding Agency	**Funding Title**			**Portion of Proposal Matched**

NSF- National Science Foundation	Simultaneous of Photoreceptor and Post-Photoreceptor Responses in the Retina			All matched
Funding Number	**Current Status**	**UIC PAF NO.**	**Performance Site**	**Funding PI**
CBET-1055889	Pending	201504507	UIC	Xincheng Yao

This institution has Animal Welfare Assurance Number A3460.01 on file with the Office of Laboratory Animal Welfare (OLAW), NIH. **This letter may only be provided as proof of IACUC approval for those specific funding sources listed above in which all portions of the funding proposal are matched to this ACC protocol.**

In addition, all investigators are responsible for ensuring compliance with all federal and institutional policies and regulations related to use of animals under this protocol and the funding sources listed on this protocol. Please use OLAW's "*What Investigators Need to Know about the Use of Animals*" (http://grants.nih.gov/grants/olaw/InvestigatorsNeed2Know.pdf) as a reference guide. Thank you for complying with the Animal Care Policies and Procedures of UIC.

Sincerely yours,

Bradley Merrill, PhD
Chair, Animal Care Committee

BM/*mbb*
cc: BRL, ACC File, Jin-Hong (Robert) Chang, PAF 201503177, 20150317, 201504507

Permission to use Figs. 1.1(a), 1.1(b), and 1.3.

Webvision

The Organization of the Retina and Visual System

About/FAQ

Q: What is Webvision? **A:** Webvision was one of the first, if not *the* first online textbook. It has since evolved into an interactive, dynamic blog hosted on WordPress that covers all things related to the bioscience of the visual system.

Q: Can I use images and/or content from Webvision? What is the copyright? **A:** All copyright for chapters belongs to the individual authors who created them. However, for non-commercial, academic purposes, images and content from the chapters portion of Webvision may be used with a non-exclusive rights under a Attribution, Noncommercial, No Derivative Works Creative Commons license. Cite Webvision, http://webvision.med.utah.edu/ as the source. Commercial applications need to obtain license permission from the administrator of Webvision and are generally declined unless the copyright owner can/wants to donate or license material. Use online should be accompanied by a link back to the original source of the material. All imagery or content associated with blog posts belong to the authors of said posts, except where otherwise noted.

Permission to use Fig. 1.1(c).

Licensing   [edit]

Permission to use Fig. 1.2.

Size of this preview: 800 × 338 pixels. Other resolutions: 320 × 135 pixels | 640 × 271 pixels | 1,327 × 561 pixels.
Original file (1,327 × 561 pixels, file size: 344 KB, MIME type: image/png)

	Open in Media Viewer	⚙

Description	Representation of molecular steps in photoactivation (modified from Leskov et al., 2000). Depicted is an outer membrane disk in a rod. Step 1: Incident photon (hv) is absorbed and activates a rhodopsin by conformational change in the disk membrane to R*. Step 2: Next, R* makes repeated contacts with transducin molecules, catalyzing its activation to G* by the release of bound GDP in exchange for cytoplasmic GTP. The α and γ subunits Step 3: G* binds inhibitory γ subunits of the phosphodiesterase (PDE) activating its α and β subunits. Step 4: Activated PDE hydrolyzes cGMP. Step 5: Guanylyl cyclase (GC) synthesizes cGMP, the second messenger in the phototransduction cascade. Reduced levels of cytosolic cGMP cause cyclic nucleotide gated channels to close preventing further influx of Na+ and Ca2+.
Date	10 December 2007
Source	http://en.wikipedia.org/wiki/File:Phototransduction.png
Author	Jason J. Corneveaux, wiki user: Caddymob (talk)
Permission (Reusing this file)	**I, the copyright holder of this work, hereby publish it under the following licenses:**

Permission to use Fig. 1.6.

Permission to use Chapters II and III.

Copyright, Permissions and Reprints

Copyright Transfer | Author Posting Policy | NIH Public Access Policy

OSA asks all authors of articles for its journals, magazines, and books to sign a Transfer of Copyright. In doing so, an author transfers ownership of his or her article or book to OSA. Ownership of copyright gives OSA the right to publish the article and to defend against improper use (or even theft) of the article. It also permits OSA to mount the article online or to use the article in other forms, such as when a journal article becomes part of a content collection or another derivative product.

OSA needs copyright for an article because, as publisher, the society is in the best position to defend the article legally. In addition, transfer of copyright assures OSA that the work in question is entirely the author's own. Once again, the purpose of transfer of copyright is not to prevent the author from reuse of his or her own work, as long as this doesn't involve republication in a competing journal or other competing resource.

If you are planning to send a manuscript to one of OSA's peer-reviewed journals, you will be given the opportunity during submission to agree to our electronic transfer of copyright. You should print and send a hard copy of the below Transfer of Copyright form only if you are unwilling or unable to use the online option.

- OSA Copyright Transfer Agreement (PDF)
- Photonics Research Copyright Transfer Agreement (PDF)

Permission to use Chapter IV.

Conference Proceedings

Journals

SPIE Digital Library

Books

Open Access

◢ Contact SPIE Publications

◢ **Reprint Permission**

Conference Content Management+Publication Services

Shipping Info

Terms of Use

Reprint Permission

If you are seeking permission to use previously published material, please contact reprint_permission@spie.org. In your e-mail, please include the following information:

- Title and author
- Volume, issue, and page numbers
- What you would like to reproduce
- Where you will republish the requested material.

Requests may also be faxed to SPIE at +1 360 647 1445 (Attention: Reprint Permissions).

Information for authors reproducing their own SPIE material

As stated in the SPIE Transfer of Copyright agreement, authors, or their employers in the case of works made for hire, retain the following rights:

1. All proprietary rights other than copyright, including patent rights.
2. The right to make and distribute copies of the Paper for internal purposes.
3. The right to use the material for lecture or classroom purposes.
4. The right to prepare derivative publications based on the Paper, including books or book chapters, journal papers, and magazine articles, provided that publication of a derivative work occurs subsequent to the official date of publication by SPIE.

Thus, authors may reproduce figures and text in new publications. The SPIE source publication should be referenced.

VITA

NAME:	BENQUAN WANG
EDUCATION:	B.E., Biomedical Engineering, Tianjin University, Tianjin, China, 2012

EDUCATION: (continued)

Ph.D., Biomedical Engineering, University of Alabama at Birmingham, Birmingham, Alabama, 2014

Ph.D., Bioengineering, University of Illinois at Chicago, Chicago, Illinois, 2017

AWARDS: Alabama EPSCoR Graduate Research Scholars Program, University of Alabama at Birmingham, 2014

PUBLICATIONS: B. Wang, Y. Lu, and X. Yao, In vivo optical coherence tomography of stimulus evoked intrinsic optical signals in mouse retinas. *Journal of Biomedical Optics* 21(9), 096010 (2016)

B. Wang, R. Lu, Q. Zhang, and X.C. Yao. Functional optical coherence tomography reveals transient phototropic change of photoreceptor outer segments. *Optics Letters* 39, 6923–6926 (2014)

B. Wang, R. Lu, Q. Zhang and X. Yao. Breaking diffraction limit of lateral resolution in optical coherence tomography, *Quantitative Imaging in Medicine and Surgery* 3, 243-248 (2013)

B. Wang, R. Lu, Q. Zhang, Y. Jiang and X. Yao. En face optical coherence tomography of transient light response at photoreceptor outer segments in living frog eyecup, *Optics Letters* 38, 4526-4529 (2013)

R. Lu, B. Wang, Q. Zhang, and X. Yao. Super-resolution scanning laser microscopy through virtually structured detection, *Biomedical Optics Express* 4, 1673-1682 (2013)

D. Thapa, B. Wang, Y. Lu, T. Son, and X. Yao, Enhancement of intrinsic optical signal recording with split spectrum optical coherence tomography, *Journal of Modern Optics* (2017)

Y. Lu, B. Wang, D. R. Pepperberg, and X. Yao, Stimulus-evoked outer segment changes occur before the hyperpolarization of retinal photoreceptors, *Biomedical Optics Express* 8 (1), 38-47 (2017)

C. Liu, Y. Zhi, B. Wang, D. Thapa, Y. Chen, M. Alam, Y. Lu and X. Yao, *In vivo* super-resolution retinal imaging through virtually structured detection, *Journal of Biomedical Optics* 21 (12), 120502-120502 (2016)

T. Son, B. Wang, D. Thapa, Y. Lu, Y. Chen, D. Cao, and X. Yao, Optical coherence tomography angiography of stimulus evoked hemodynamic responses in individual retinal layers, *Biomedical Optics Express* 8, 3151-3162 (2016)

X. Zhao, D. Thapa, B. Wang, Y. Lu, S. Gai and X. Yao. Stimulus-evoked outer segment changes in rod photoreceptors. *Journal of Biomedical Optics* 21(6):065006 (2016)

X. Yao and B. Wang, Intrinsic optical signal imaging of retinal physiology: a review. *Journal of Biomedical Optics* 20, 090901 (2015)

Y. Zhi, B. Wang, and X. Yao. Super-resolution scanning laser microscopy based on virtually structured detection. *Critical Reviews in Biomedical Engineering* 43:4 297-322 (2015)

Q. Zhang, R. Lu, B. Wang, J. D. Messinger, C. A. Curcio, and X.C. Yao. Functional optical coherence tomography enables *in vivo* physiological assessment of retinal rod and cone photoreceptors. *Scientific Reports* 5, 9595 (2015)

Y. Zhi, R. Lu, B. Wang, Q. Zhang, and X.C. Yao. Rapid super-resolution line scanning microscopy through virtually structured detection. *Optics Letters* 40, 1683-1686 (2015)

R. Lu, Y. Zhi, B. Wang, Q. Zhang, and X.C. Yao. A polarization-sensitive light field imager for multi-channel angular spectroscopy of light scattering in biological tissues. *Quantitative Imaging in Medicine and Surgery* 5, 1-8 (2015)

PRESENTATIONS: Benquan Wang, Devrim Toslak, and Xincheng Yao. Nonmydriatic single-shot widefield fundus camera with trans-pars planar illumination. *ARVO Imaging in the Eye Conference*. Baltimore, MD. May 2017.

Benquan Wang and Xincheng Yao. *In vivo* Functional Optical Coherence Tomography of Fast Intrinsic Optical Signals in Mouse Retina. SPIE Photonics West. San Francisco, CA. February 2016.

Qiuxiang Zhang, Rongwen Lu, Benquan Wang, Jeffrey D. Messinger, Christine A. Curcio, and Xincheng Yao. In-vivo Functional Optical Coherence Tomography of Fast Intrinsic Optical Signals in Frog Retina. SPIE Photonics West. San Francisco, CA. February 2015.

Benquan Wang, Rongwen Lu, Qiuxiang Zhang and Xincheng Yao. En face Optical Coherence Tomography of Transient Light Response at Photoreceptor Outer Segments in Living Frog Eyecup. ARVO Annual Meeting. Orlando, FL. May 2014. (Hot topic)